

Segment-scale and intrasegment lithospheric thickness and melt variations near the Andrew Bain megatransform fault and Marion hot spot: Southwest Indian Ridge, 25.5°E-35°E

Christopher Takeuchi, John Sclater, Nancy Grindlay, John Madsen, Céline Rommevaux-Jestin

▶ **To cite this version:**

Christopher Takeuchi, John Sclater, Nancy Grindlay, John Madsen, Céline Rommevaux-Jestin. Segment-scale and intrasegment lithospheric thickness and melt variations near the Andrew Bain megatransform fault and Marion hot spot: Southwest Indian Ridge, 25.5°E-35°E. Geochemistry, Geophysics, Geosystems, 2010, 11 (7), 10.1029/2010GC003054 . insu-01777854

HAL Id: insu-01777854
https://insu.hal.science/insu-01777854

Submitted on 6 Aug 2020

HAL is a multi-disciplinary open access archive for the deposit and dissemination of scientific research documents, whether they are published or not. The documents may come from teaching and research institutions in France or abroad, or from public or private research centers.

L'archive ouverte pluridisciplinaire **HAL**, est destinée au dépôt et à la diffusion de documents scientifiques de niveau recherche, publiés ou non, émanant des établissements d'enseignement et de recherche français ou étrangers, des laboratoires publics ou privés.

Geochemistry Geophysics Geosystems G3

Article
Volume 11, Number 7
21 July 2010
Q07012, doi:10.1029/2010GC003054
ISSN: 1525-2027

Published by AGU and the Geochemical Society



Segment-scale and intrasegment lithospheric thickness and melt variations near the Andrew Bain megatransform fault and Marion hot spot: Southwest Indian Ridge, 25.5°E–35°E

Christopher S. Takeuchi and John G. Sclater
Scripps Institution of Oceanography, University of California, San Diego, La Jolla, California 92093, USA (ctakeuch@ucsd.edu)

Nancy R. Grindlay
Department of Geography and Geology, University of North Carolina at Wilmington, Wilmington, North Carolina 28403, USA

John A. Madsen
Department of Geological Sciences, University of Delaware, Newark, Delaware 19716, USA

Céline Rommevaux-Jestin
Institut de Physique du Globe du Paris, UMR 7154, CNRS, F-75252 Paris, France

[1] We analyze bathymetric, gravimetric, and magnetic data collected on cruise KN145L16 between 25.5°E and 35°E on the ultraslow spreading Southwest Indian Ridge, where the 750 km long Andrew Bain transform domain separates two accretionary segments to the northeast from a single segment to the southwest. Similar along-axis asymmetries in seafloor texture, rift valley curvature, magnetic anomaly amplitude, magnetization intensity, and mantle Bouguer anomaly (MBA) amplitude within all three segments suggest that a single mechanism may produce variable intrasegment lithospheric thickness and melt delivery. However, closer analysis reveals that a single mechanism is unlikely. In the northeast, MBA lows, shallow axial depths, and large abyssal hills indicate that the Marion hot spot enhances the melt supply to the segments. We argue that along-axis asthenospheric flow from the hot spot, dammed by major transform faults, produces the inferred asymmetries in lithospheric thickness and melt delivery. In the southwest, strong rift valley curvature and nonvolcanic seafloor near the Andrew Bain transform fault indicate very thick subaxial lithosphere at the end of the single segment. We suggest that cold lithosphere adjacent to the eastern end of the ridge axis cools and thickens the subaxial lithosphere, suppresses melt production, and focuses melt to the west. This limits the amount of melt emplaced at shallow levels near the transform fault. Our analysis suggests that the Andrew Bain divides a high melt supply region to the northeast from an intermediate to low melt supply region to the southwest. Thus, this transform fault represents not only a major topographic feature but also a major melt supply boundary on the Southwest Indian Ridge.

Components: 14,500 words, 12 figures, 1 table.

Keywords: Southwest Indian Ridge; Andrew Bain; ultraslow spreading; melt supply.

Index Terms: 3035 Marine Geology and Geophysics: Midocean ridge processes; 3045 Marine Geology and Geophysics: Seafloor morphology, geology, and geophysics; 9340 Geographic Location: Indian Ocean.

Received 20 January 2010; **Revised** 27 April 2010; **Accepted** 20 May 2010; **Published** 21 July 2010.

Copyright 2010 by the American Geophysical Union

Takeuchi, C. S., J. G. Sclater, N. R. Grindlay, J. A. Madsen, and C. Rommevaux-Jestin (2010), Segment-scale and intrasegment lithospheric thickness and melt variations near the Andrew Bain megatransform fault and Marion hot spot: Southwest Indian Ridge, 25.5°E–35°E, *Geochem. Geophys. Geosyst.*, *11*, Q07012, doi:10.1029/2010GC003054.

1. Introduction

[2] Extensive knowledge of the processes by which oceanic lithosphere and crust is formed has been gained from studies of the fast spreading East Pacific Rise [e.g., *Macdonald et al.*, 1984; *Sempéré and Macdonald*, 1986; *Madsen et al.*, 1990] and the slow spreading Mid-Atlantic Ridge (MAR) [e.g., *Kuo and Forsyth*, 1988; *Lin et al.*, 1990; *Blackman and Forsyth*, 1991; *Rommevaux et al.*, 1994; *Detrick et al.*, 1995]. Recent studies on the Southwest Indian Ridge (SWIR) and Gakkel Ridge have led to the definition of a new spreading regime with unique lithospheric and crustal characteristics: the ultraslow (<20 mm/yr full rate) spreading ridge [*Dick et al.*, 2003; *Cannat et al.*, 2003].

[3] Topography, gravity, and geochemical sampling have all provided evidence for the highly variable nature of melt supply on the SWIR at both regional (>200 km) and segment length (<200 km) scales. The regional melt supply of a spreading ridge is largely controlled by mantle temperature, composition, and upwelling velocity, the last of which is directly tied to the spreading rate [*Reid and Jackson*, 1981]. At spreading rates below 20 mm/yr (i.e., at ultraslow spreading ridges), conductive cooling strongly inhibits melting and thus crustal production [*Bown and White*, 1994; *White et al.*, 2001; *Dick et al.*, 2003], though this effect is likely tempered at such rates due to the focusing and acceleration of mantle upwelling [*White et al.*, 2001]. Regional ridge obliquity also influences melt supply; increased obliquity decreases the effective spreading rate (the component of the spreading velocity orthogonal to the ridge) and thus also the mantle upwelling rate and melt supply [*Dick et al.*, 2003; *Montési and Behn*, 2007].

[4] Regional axial depth and the sodium content of basaltic crust (and other geochemical indicators of partial melting) may be interpreted to reflect variable regional melt supply to a spreading ridge [*Klein and Langmuir*, 1987; *Cannat et al.*, 2008]. Mean axial depth, if assumed to be the product of isostatically balanced crust, and basaltic sodium content both decrease as melt supply increases [*Klein and Langmuir*, 1987]. These observations have been invoked to infer a broad-scale decrease in melt supply from the shallow, low sodium content SWIR axis between the Prince Edward and Discovery II transform faults (35.55°E–41.53°E) to the deep, high sodium content axis near the Rodrigues Triple Junction [*Cannat et al.*, 2008].

[5] While regional melt supply is largely a function of upwelling mantle velocity, temperature, and composition, the delivery of melt to individual segments is heavily influenced by a number of shallow processes. The most prominent of these processes involves discontinuities, both transform and nontransform, that offset the ridge axis. The juxtaposition of cold lithosphere across discontinuities and against the ends of ridge segments cools and thickens the subaxial lithosphere, which can suppress melting processes underneath the ridge [*Fox and Gallo*, 1984; *Magde and Sparks*, 1997]. Melt can also be strongly focused away from the discontinuities along the sloping base of the lithosphere, with longer discontinuities focusing melt more intensely [*Magde et al.*, 1997; *Magde and Sparks*, 1997]. The juxtaposition also produces a weld between the lithospheric sections on either side of the discontinuity. The weld produces a rotation of the horizontal stress field at the RTI due to the interplay between normal stresses at the ridge axis and shear stresses along the adjacent transform fault [*Fujita and Sleep*, 1978; *Phipps Morgan and Parmentier*, 1984]. As a result, rift valley normal faults, which initiate orthogonally to the axis of the maximum tensile stress, form at angles increasingly oblique to the spreading direction as the transform fault is approached, which causes the rift valley to curve into the transform fault.

[6] On the SWIR, segment obliquity also affects lithospheric thickness and the amount of melt delivered to the ridge axis. Thick lithosphere under oblique segments can prevent fracturing, which keeps melt from reaching the seafloor [*Montési and Behn*, 2007]; this melt is either trapped in the lithosphere or migrates along axis to an orthogonal segment [*Cannat et al.*, 2003, 2008]. This segment-to-segment melt migration represents a fundamental difference in melt delivery variations between the SWIR and MAR; while MAR segments all receive a volume of melt roughly equal to the regional average, SWIR segment melt delivery is highly spatially variable, with some segments receiving

more melt than the regional average, some receiving less [*Cannat et al.*, 2008].

[7] In February and March 1996, investigators conducted the first geophysical survey of the SWIR between 15°E and 35°E [*Grindlay et al.*, 1996]. Bathymetric, gravimetric, and magnetic data were collected over roughly 1500 km of the SWIR on cruise KN145L16. *Grindlay et al.* [1998] studied the bathymetric and gravimetric segmentation of the nearly linear, transform fault-free supersegment between 15°E and 25°E. *Dulaney* [2002] investigated the axial morphology of the entire survey region. *Sclater et al.* [2005] examined the Andrew Bain megatransform fault, which lies between 28°E and 32°E. In this study, we investigate the SWIR immediately adjacent to the major topographic boundary of the Andrew Bain fracture zone. We incorporate two surveys on either side of the Andrew Bain, between 25.5°E and 28°E, and between 32°E and 35°E. This data fills in the last major section of the SWIR not previously reported (see references of *Cannat et al.* [2008]). We use the morphology, mantle Bouguer anomaly, magnetic anomalies, and magnetization intensity to establish the segmentation patterns of the two areas surveyed. We utilize the observations to infer mechanisms that may produce variations in lithospheric thickness and the volume of melt delivered to and emplaced within segments. We also use our data to establish the Andrew Bain transform fault as a major melt supply boundary.

2. Tectonic Setting and Regional Background

[8] The SWIR is the divergent plate boundary between the Antarctic and Nubian/Somalian plates. The SWIR has a total length of 7700 km; it is offset, almost exclusively in a left-stepping sense, by transform faults and higher-order discontinuities. The ridge has an average full spreading rate of ~12–18 mm/yr [*Chu and Gordon*, 1999], the slowest rate of any readily accessible mid-ocean ridge axis. Only the ice-covered Gakkel Ridge spreads more slowly, diverging at a full rate of 8–13 mm/yr [*Cochran et al.*, 2003; *Dick et al.*, 2003].

[9] Between 25°E and 35°E, the SWIR is partitioned four times by the right-lateral, left-stepping Du Toit, Andrew Bain, Marion, and Prince Edward transform faults. These four transform faults offset the SWIR over 1100 km [*Fisher and Goodwille*, 1997] (Figure 1). This is the only section all along the SWIR where the offset is achieved almost exclusively by transform faults. At other locations on the SWIR, the northward offset of the ridge axis is achieved by transform faults, oblique spreading [*Mendel et al.*, 1997; *Dick et al.*, 2003], nontransform discontinuities [*Grindlay et al.*, 1998; *Sauter et al.*, 2001], or any combination thereof [*Baines et al.*, 2007].

[10] With a length of ~750 km and a maximum width of 120 km, the Andrew Bain transform domain dominates the morphology of this section of the SWIR. The Andrew Bain transform domain is second in offset length to only the Romanche transform fault on the central Mid-Atlantic Ridge [*Sclater et al.*, 2005]. *Ligi et al.* [2002] classified the Andrew Bain as a megatransform; *Chu and Gordon* [1999] and *Lemaux et al.* [2002] have suggested that the plate boundary between the Nubian and Somalian plates intersects the SWIR in the vicinity of the Andrew Bain.

3. Data Processing and Reduction

[11] Cruise KN145L16 included two surveys between 25.5°E and 35°E, at either end of the long-offset Andrew Bain transform; the southern covered the SWIR between 25.5°E and 28°E and the northern between 32°E and 35°E. These surveys examined the axis of the SWIR and the flanking seafloor using ~105–120 km long across-axis profiles spaced 8 km apart. In addition, the southern survey included three along-axis tracks. We denote the survey areas according to the transform faults that bound them; we thus refer to the southern survey area as survey area DA, and the northern survey area as AP.

3.1. Multibeam Bathymetry

[12] Bathymetric data were acquired with a SeaBeam 2112 multibeam system, operating with a source frequency of 12 kHz. The system allowed athwartships swath coverage of 90°–120°; swath widths were routinely 11–12 km. Navigation was derived from continuous Global Positioning System fixes. The spacing of ship tracks and swath widths allowed for 90%–100% ensonification of the seafloor. The multibeam data was ping edited to remove spurious returns; noise was significant during periods of bad weather. The outer 3–5 beams on either side of each ping were usually edited out due to their high noise level.

[13] The ping-edited bathymetry data were gridded using the open source swath sonar data processing

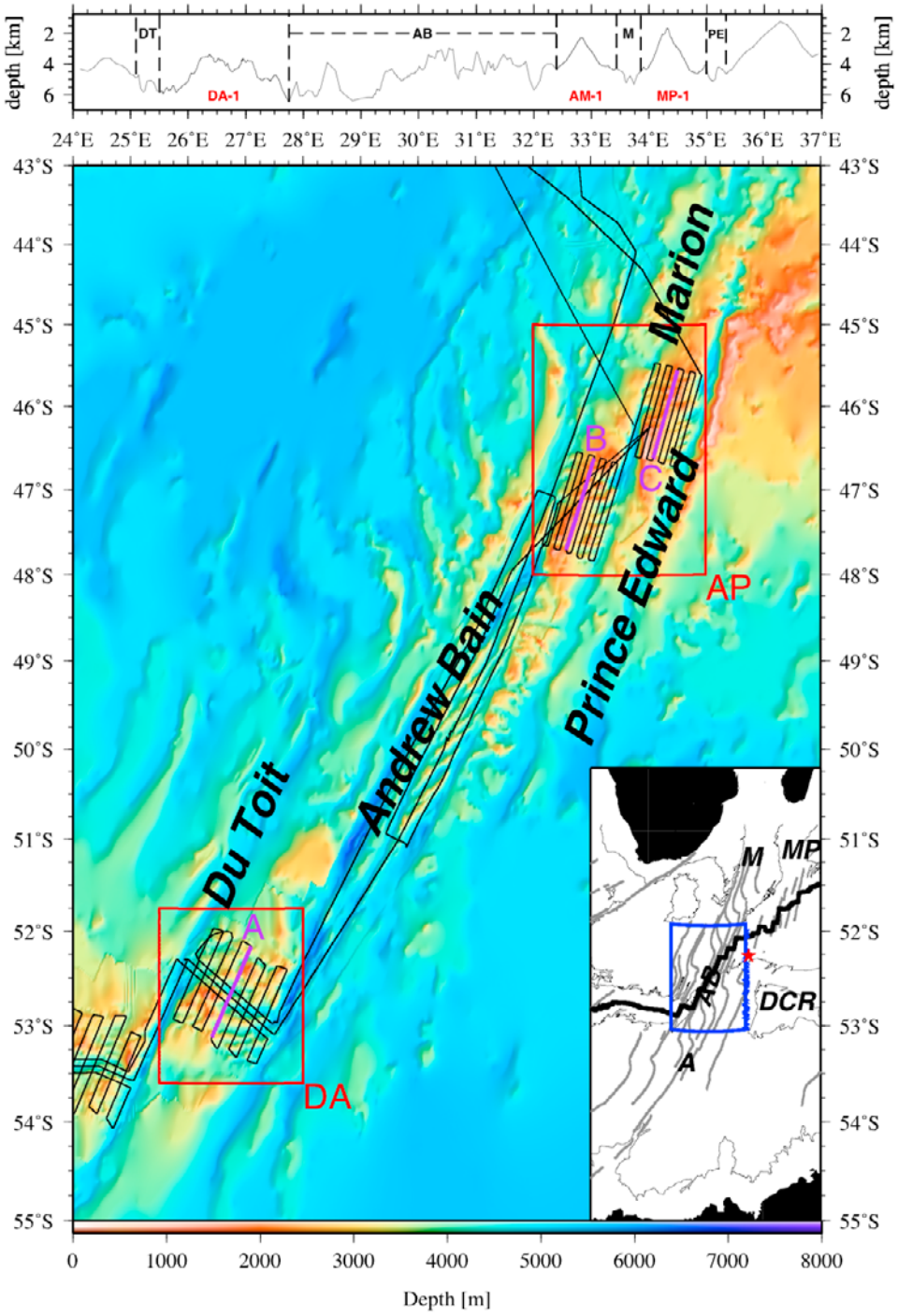


Figure 1. Shipboard bathymetry merged with the 2003 release of the GEBCO 1 min grid [*Fisher and Goodwille*, 1997] showing the SWIR between 24°E and 37°E. Du Toit, Andrew Bain, Marion, and Prince Edward transform faults are labeled. Black lines indicate track lines of cruise KN145L16. Red boxes show survey areas DA and AP (as labeled) of the present study. Purple lines indicate locations of magnetic anomaly profiles used in Figure 2. The profile at the top shows along-axis bathymetric profile of the SWIR between 24°E and 37°E. Transform domains bounded by dashed lines and labeled as follows: DT, Du Toit; AB, Andrew Bain; M, Marion; PE, Prince Edward. Ridge segments are labeled as defined in section 6. In the inset, thick black line denotes crest of SWIR; grey lines denote SWIR fracture zone traces. Thin grey lines indicate 4000 m bathymetric contour. A, AB, DCR, M, and MP denote the Astrid Fracture Zone, Andrew Bain transform fault, Del Cano Rise, Mozambique Escarpment, and Madagascar Plateau, respectively. Red star denotes location of Marion Island. Blue box shows area covered by Figure 1.

code MB-System [*Caress and Chayes*, 1996]. Using MB-System, we calculated the value of each grid cell by taking a Gaussian weighted average of the values at surrounding data points. The bathymetry data were gridded with an interval of 50 m to allow for a thorough analysis of seafloor texture. We utilized a 2-D thin plate spline interpolation to fill in the gaps between individual pings, which were frequent due to the rough weather common to the area. However, we did not fill in gaps between ship tracks in order to be certain that our seafloor texture analysis was controlled by data rather than interpolation artifacts.

3.2. Gravity Data

[14] Gravity data were collected using a Bell BGM-3 gravimeter. The data were merged with the GPS navigation and center beam bathymetry to provide synchronized gravity and bathymetry data. The Eötvös correction was then applied, and a reference gravity value was removed to obtain free-air anomalies. This reference gravity value was calculated using

$$\text{ref. gravity} = 978049.0 * (1.0 + 0.0052884 * \sin^2(\text{lat}) - 0.0000059 * \sin^2(2 * \text{lat})),$$

where "lat" was the ship's latitude in degrees. The data were edited to remove spurious points and points recorded during ship turns, smoothed by the application of a 13-point (~2–3 min of time) running mean filter, and linearly interpolated to evenly spaced 1 min (time) values. To obtain estimates of the gravimeter drift, measurements were taken at base stations in Durban and Cape Town, South Africa (the departure and arrival ports, respectively), and then referenced to the values recorded on the ship. A DC correction of −2.1 mGal was also applied to the data to account for the difference between the gravity measured at the base station in Durban and that recorded on the ship prior to departure. Crossover error analysis was completed using the GMT supplement "xsystem" software [*Wessel and Smith*, 1998]. The gravity data had crossover errors with a mean of 2.0 mGal and a standard deviation of 2.6 mGal.

[15] We calculated mantle Bouguer anomalies (MBAs) following the method of *Prince and Forsyth* [1988]. We added additional bathymetric spline interpolation to fill in data gaps between ship tracks. We then extended the shipboard bathymetry data beyond the two ridge axis survey areas using the 2003 release of the GEBCO 1 min grid of *Fisher and Goodwille* [1997]; the composite bathymetry data was also gridded with a 1 min interval to match the resolution limit of the GEBCO grid. We utilized the *Parker* [1973] Taylor series method to convert the topography to the gravitational signal due to interfaces between layers of seawater (1 g cm^{-3}), upper crust (2 km thick, 2.4 g cm^{-3}), lower crust (4 km thick, 2.7 g cm^{-3}), and mantle (3.3 g cm^{-3}). In order to minimize edge effects caused by the periodicity assumed in the Fast Fourier Transform (FFT) calculations of the *Parker* [1973] method, we mirrored the topography at the edges of our domain. The calculated gravity contributions of the interface topography were then gridded at an interval of 1 min using the GMT software adjustable curvature algorithm "surface" [*Wessel and Smith*, 1998] with a tension factor of 0.25. We then sampled the gravity contribution grids at locations along ship tracks at which free air gravity data existed; the sampled values were then removed from the free air gravity, producing values of MBA along ship tracks. The MBA data were gridded at 1 min resolution using "surface" [*Wessel and Smith*, 1998] with a tension factor of 0.25.

3.3. Magnetic Data

[16] Magnetic data were collected with a Geometrics G-886 Marine Magnetometer. The International Geomagnetic Reference Field (IGRF 6th Generation [*Langel*, 1992]; the magnetic reduction was completed immediately following the cruise) was removed from the raw magnetic field data to produce magnetic anomalies. The magnetometer logging interval changed during the cruise, so the magnetic anomalies were interpolated using a weighted mean to produce evenly spaced 1 min (time) values. Crossover error analysis was again completed using "xsystem" [*Wessel and Smith*, 1998]; crossover errors had a mean of 0.5 and a standard deviation of 25.8 nT.

[17] We utilized two-dimensional forward modeling in order to identify the magnetic anomaly reversal pattern. We reduced the observed magnetic anomalies to the pole to remove the effects of skewness due to latitude. We ran a forward model using a 1 km thick magnetized layer, bounded on top by the bathymetry, with a magnetization distribution based on a square wave function constructed with the *Cande and Kent* [1995] geomagnetic time scale. We assumed a 10 A/m magnetization for the Brunhes normal polarity period (0–0.78 Ma) and a 2 A/m intensity off axis. The best fit between the synthetic and reduced-to-the-pole anomaly patterns was achieved using a 13–16.2 km/Myr

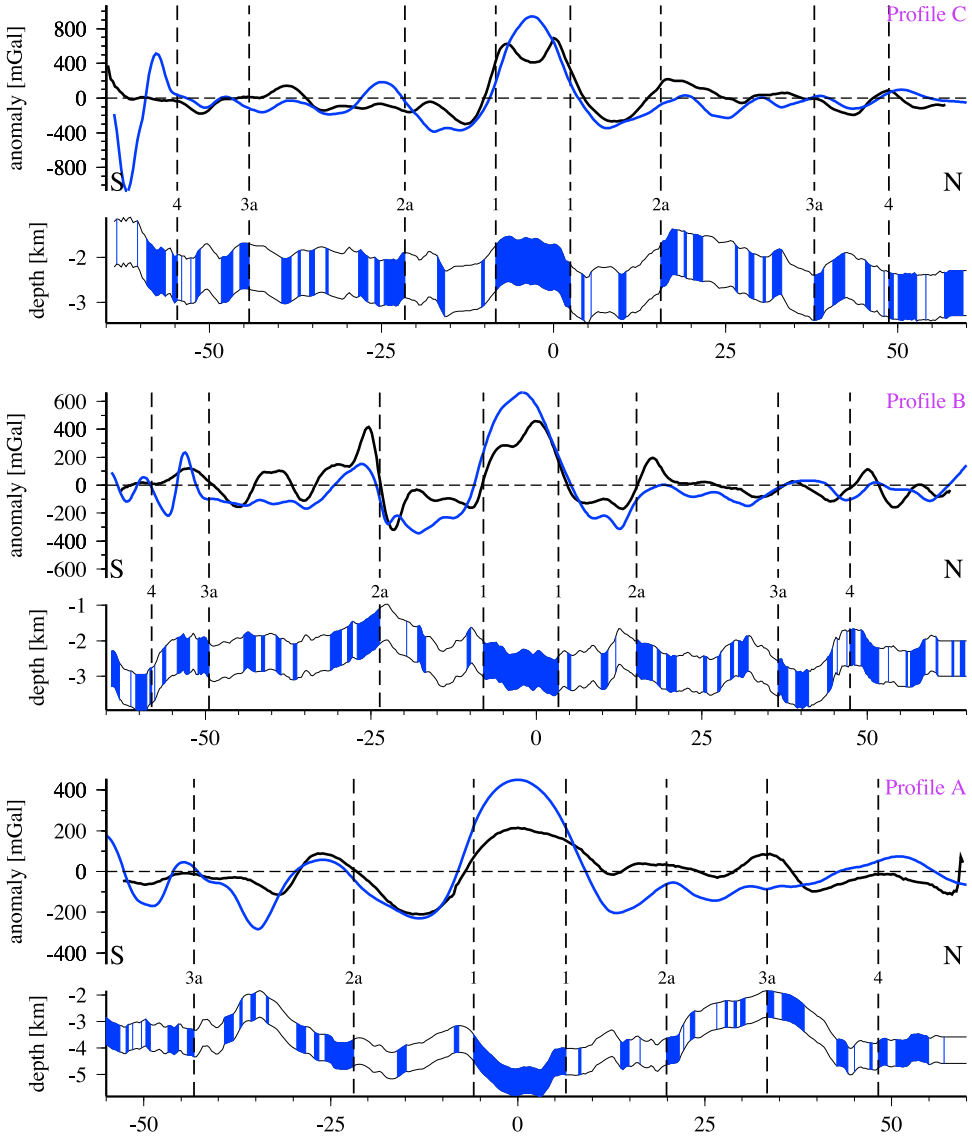


Figure 2. Identification of magnetic anomalies along profiles A, B, and C. Locations are indicated by purple lines in Figure 1. Reduced-to-the pole magnetic anomalies are plotted in black, and synthetic anomalies are plotted in blue. Synthetic anomaly profiles are calculated from a two-dimensional block model based on the *Cande and Kent* [1995] geomagnetic time scale, with 13–16.2 km/Myr full spreading rates and 0%–25% spreading asymmetries. The forward model assumes a 1 km thick magnetic source layer with a magnetization intensity of 10 A/m for the Brunhes period and 2 A/m off axis. S and N refer to south and north.

spreading rate with 0%–25% spreading asymmetries (Figure 2).

[18] We performed a three-dimensional inversion of the observed magnetic anomaly data using the two-dimensional method of *Parker and Huestis* [1974], extended to three dimensions by *Macdonald et al.* [1980]. We used a 1 km thick magnetic source layer, bounded on top by the same composite bathymetry grid used in the MBA calculations. A cosine taper band-pass filter with a low-cut taper from 150 to 300 km and a high-cut taper from 4 to 8 km assured convergence of the inversion. As with the MBA calculation, we mirrored the topography at the edges to minimize edge effects caused by the assumed periodicity of the FFT calculations in the inversion. We assumed a crustal magnetization parallel to a geocentric axial dipole. The magnetization data were gridded at a resolution of 1 min to match the resolution limit of the composite bathymetry grid.

[19] We did not add any magnetic annihilator to the result of our inversion for a number of reasons. As

shown by *Tivey and Tucholke* [1998], the water depth filter and narrow polarity reversal spacing preclude the ability of sea surface magnetic observations to resolve well the amplitude of magnetization anomalies on seafloor created at slow spreading rates. As such, for slow spreading rates, balancing positive and negative amplitudes across reversal boundaries is not an appropriate technique for calculating the amount of annihilator to add to a magnetization solution. However, the technique proposed by *Tivey and Tucholke* [1998] of adding annihilator so that the magnetization zero crossings on each track match those of the magnetic anomalies was also fruitless, as no constant multiple of the annihilator could successfully accomplish the matching of the zero crossings within each individual ridge segment. As such, we will focus on the relative amplitude variations of the magnetization instead of the absolute values in our analysis.

3.4. Earthquake Locations

[20] To further understand the plate boundary geometry, we supplement our shipboard data with earthquakes from the relocated epicenter database of *Engdahl et al.* [1998] (EHB). The approximately 100,000 global earthquakes of this database are a combined set of International Seismological Centre (ISC) and National Earthquake Information Center (NEIC); they cover the time period from January 1964 through March 2010. The initial ISC and NEIC hypocentral location estimates of this data set were improved using arrival times from phases *PKiKP*, *PKPdf*, *pP*, *pwP*, and *sP*, in addition to *S* and *P* phases, in the location procedure. Where available, we have plotted focal mechanisms for these earthquakes as calculated by the Global Centroid Moment Tensor (GCMT) catalog. Within our survey areas, locations for EHB events before January 1999 have an average epicentral location uncertainty of 13.0 ± 3.7 km; uncertainties for later earthquakes have not been published. However, assuming that the post-January 1999 events have a similar order of magnitude of uncertainty as the pre-January 1999 events, the uncertainties preclude our ability to correlate earthquake locations to specific morphological features. We thus only utilize them to determine the general location of active spreading.

4. Survey Area AP: 32°E–35°E

4.1. Morphology

4.1.1. Rift Valley

[21] Survey area AP shows two very similar morphological sectors bounded by three transform faults (Figure 3). The southwestern of these two sectors, lying between the Andrew Bain and Marion transform faults, has a rift valley with a length of ~85 km. On its western end, the valley strikes 102° and intersects nearly orthogonally with the Andrew Bain transform fault; on its eastern end, the rift valley begins to curve northward ~25 km away from the Marion transform fault (Figure 3a). The center of the rift valley is filled by a large axial high (Figure 4a) that shoals to a water depth of ~2270 m at its shallowest point. The rift valley deepens by ~2100 m to both the west and the east; however, the overall bathymetric profile is somewhat asymmetric, with the shallowest point of the central axial high located ~7 km west of the center point between the bounding transform faults. This asymmetry results in overall greater depths to the east than to the west. The mean depth of the rift valley is ~3550 m.

[22] The northeastern sector, lying between the Marion and Prince Edward transform faults, is very similar morphologically to the southwestern sector (Figure 3a). The ~85 km long rift valley in the

Figure 3. (a) The 1 min gridded bathymetry of the SWIR between 32°E and 35°E, survey area AP. Bathymetric contour interval is 500 m. Black dots denote locations of earthquake solutions [*Engdahl et al.*, 1998], with focal mechanisms plotted where available. Green dots indicate locations of dredge hauls of *Mahoney et al.* [1992], both of which recovered normal incompatible-depleted mid-ocean ridge basalts. (b) The 1 min gridded mantle Bouguer anomaly. Shipboard bathymetry has been extended beyond the survey area with the GEBCO 1 min grid [*Fisher and Goodwille*, 1997] for MBA calculations. MBA contours are in black, interval is 5 mGal, and heavy black line indicates zero MBA contour. White contours are 1000 m bathymetric contours. (c) Reduced-to-the-pole magnetic anomalies. Positive amplitudes to the west-northwest. Purple symbols indicate the center of positive polarity intervals 1 (0–0.78 Ma, diamond), 2a (2.581–3.58 Ma, triangle), 3a (5.894–6.567 Ma, circle), and 4 (7.432–8.072 Ma, inverted triangle) [*Cande and Kent*, 1995]. (d) The 1 min gridded magnetization intensity. Magnetization contours are in black, interval is 1.25 A/m, and heavy black line indicates zero magnetization contour. White contours are 1000 m bathymetric contours. Purple symbols indicate magnetic anomaly picks as in Figure 3c. Red lines in Figures 3a, 3b, and 3d indicate the location of the plate boundary. Transform fault locations are labeled in all plots as follows: AB, Andrew Bain; M, Marion; PE, Prince Edward.

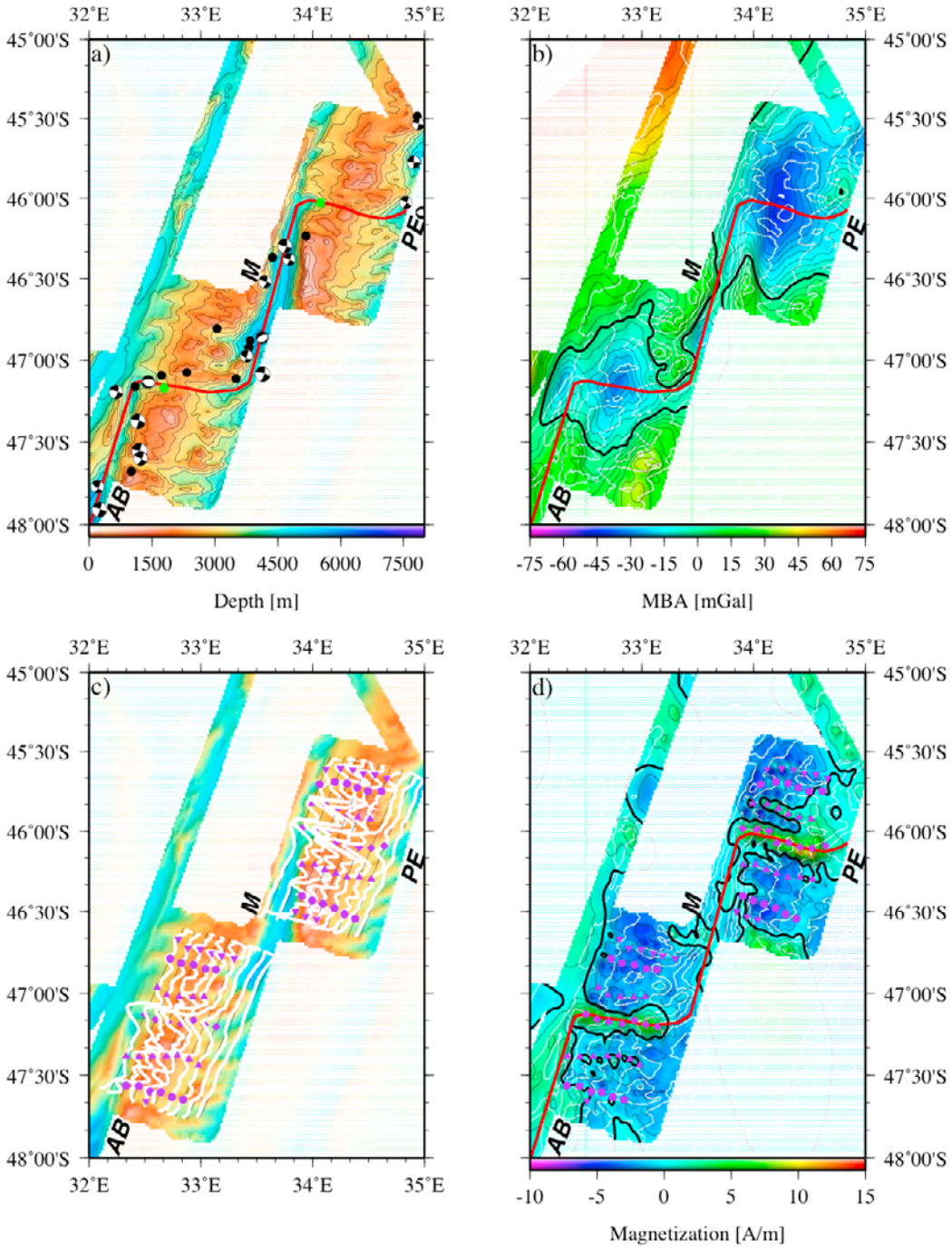


Figure 3

northwestern sector very nearly parallels that of the southwestern sector. It strikes ~102° at its western end and intersects nearly orthogonally with the Marion transform fault. The valley begins curving northward ~25 km away from the Prince Edward transform fault on its eastern end. As with the southwestern sector, the valley is filled by a large central axial high. However, this central high is shallower than that of the southwestern sector, rising to a depth of ~1700 m (Figure 4b). The rift valley also has greater relief than that of the southwestern sector, deepening by ~2800 m to the west and by ~3000 m to the east. Again, the bathymetric profile is asymmetric, with (1) the summit of the axial high located slightly (~8 km) west of the center point between the bounding

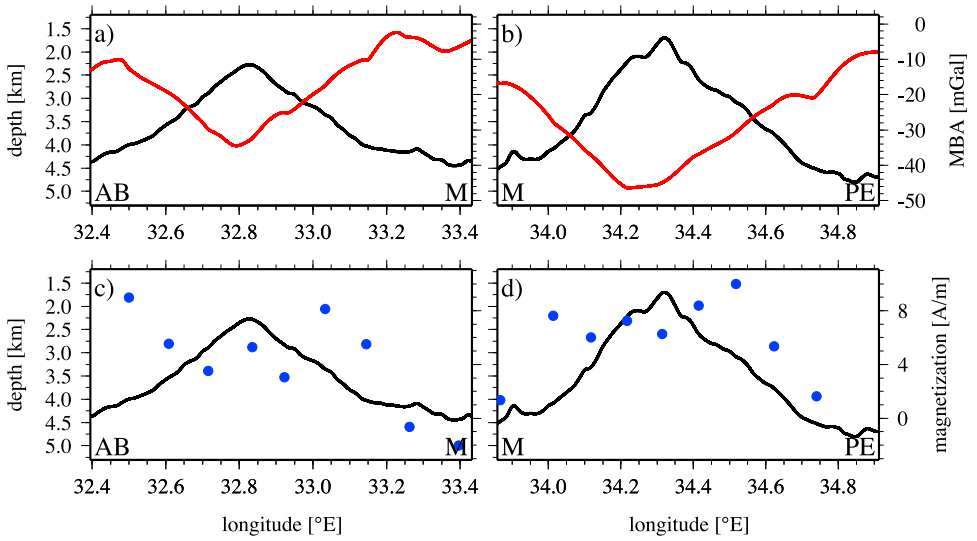


Figure 4. Along-axis bathymetry, MBA, and magnetization data for survey area AP. Fields are sampled along the plate boundary, plotted in red in Figures 3a, 3b, and 3d. Magnetization is only plotted at crossing points between the plate boundary and ship tracks due to the lack of along-axis ship track coverage within this survey area. Transform fault locations are labeled in all plots as follows: AB, Andrew Bain; M, Marion; PE, Prince Edward. (a) Bathymetry (black) and MBA (red) between the Andrew Bain and Marion transform faults. (b) Bathymetry (black) and MBA (red) between the Marion and Prince Edward transform faults. (c) Bathymetry (black) and magnetization (blue) between the Andrew Bain and Marion transform faults. (d) Bathymetry (black) and magnetization (blue) between the Marion and Prince Edward transform faults.

transform faults and (2) overall greater depths on the eastern end of the valley. The mean depth of the rift valley is ~3500 m. A small ridge lies at the far western end (Figure 4b).

4.1.2. Seafloor Texture

[23] Rift valley–parallel abyssal hill fabric dominates the topography flanking both rift valleys of survey area AP (Figure 5). These abyssal hills are quite large, rising 500–1000 m above the surrounding seafloor. The seafloor is composed exclusively of volcanic terrain, in the form of pebbly textures composed of small (<500 m diameter), roughly circular constructs akin to hummocky pillow lava flows seen observed with TOBI side scan imagery [*Sauter et al.*, 2002, 2004b] (hereafter referred to as hummocky terrain), flat-topped mounds, and ridge axis–parallel scarps. Along-axis asymmetries in the density of mounds are observed, with more found near the western bounding transform faults than near the eastern transform faults (Figure 6).

4.2. Mantle Bouguer Anomaly

[24] The gravity data show a broad, roughly circular MBA low centered near the central axial high of each rift valley of survey area AP (Figure 3b). The MBA lows are somewhat elongated perpendicular to these valleys. Between the Andrew Bain and Marion transform faults, the minimum of −35 mGal is located near the summit of the central axial high. The MBA increases westward by 22 mGal and eastward by 30 mGal (Figure 4a). Between the Marion and Prince Edward transform faults, the gravity data show a broad elliptical −47 mGal MBA low centered near the summit of the central axial high (Figure 4b). The MBA increases westward by 30 mGal and eastward by 38 mGal. The MBA of the northeastern sector thus has greater (i.e., more negative) amplitude and greater along-axis variation than that of the southwestern sector. Both MBA lows have asymmetric profiles inversely correlated to the topography of the two sectors, with lower overall amplitudes in the west relative to the east.

4.3. Magnetization and Magnetic Anomalies

[25] Survey area AP has strong central magnetic anomaly highs and central anomaly magnetization highs (CAMHs [*Klitgord*, 1976]) over each of two rift valleys, with the northeastern sector showing a greater peak and average amplitude (Figures 3c and 3d). Both the magnetic anomalies and magnetization distribution generally show identifiable mag-

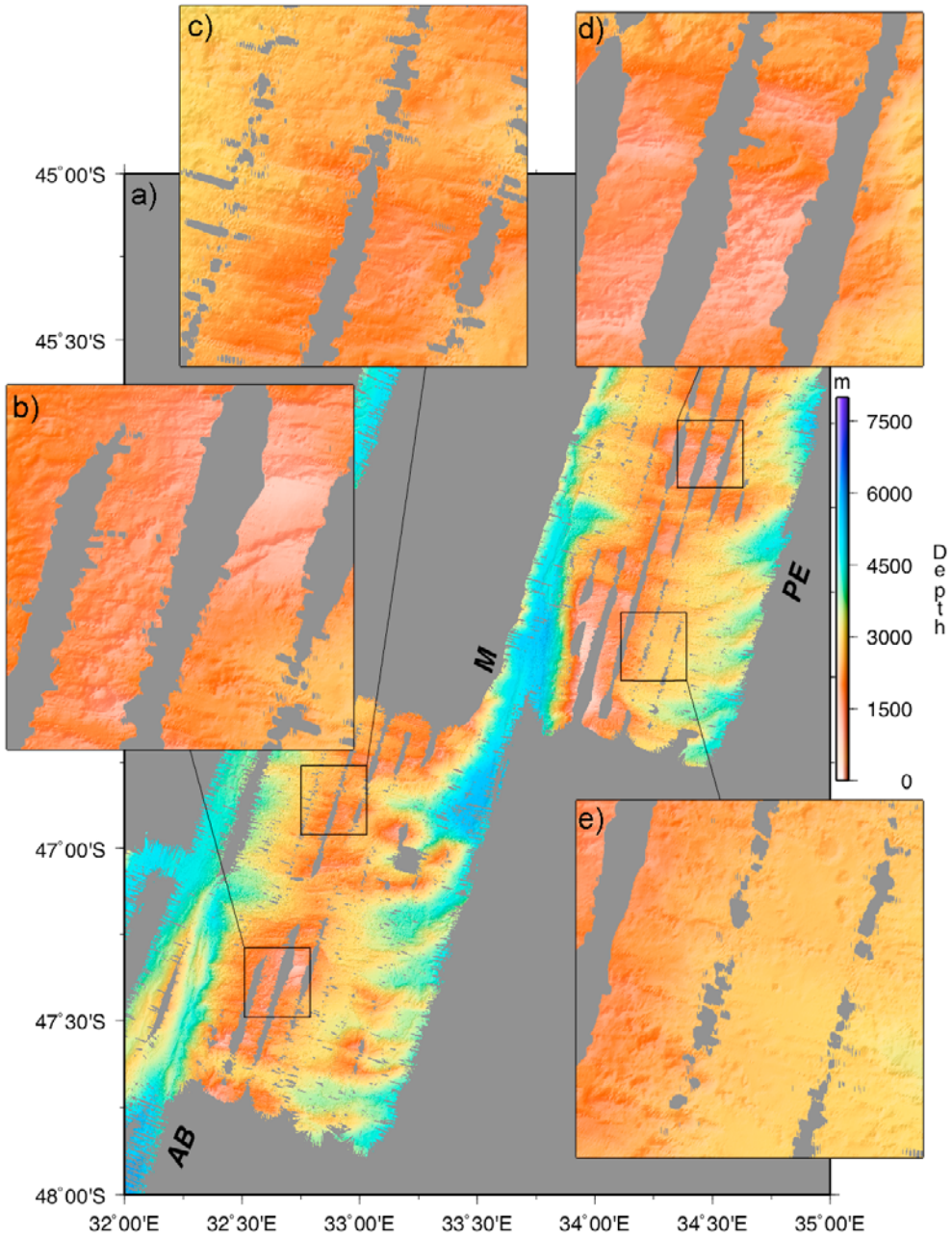


Figure 5. (a) High-resolution shipboard bathymetry (50 m grid interval) of the SWIR between 32°E and 35°E, survey area AP, showing volcanic terrain and abyssal hill fabric. Illumination is from the west-northwest. Grey areas are between-track data gaps. Transform fault locations are labeled in Figure 5a as follows: AB, Andrew Bain; M, Marion; PE, Prince Edward. (b) Southern flank and (c) northern flank of the ridge axis between the Andrew Bain and Marion transform faults. (d) Northern flank and (e) southern flank of the ridge axis between the Marion and Prince Edward transform faults.

netic lineations corresponding to alternating polarity intervals. However, asymmetries exist that parallel those observed in the bathymetry and gravity data. The magnetic lineation patterns are clear within 5 km of the western bounding transform faults of both the southwestern and northeastern sectors. However, on the eastern end of each sector, the lineation patterns disappear and amplitudes become flat near where the rift valleys begin to curve into the eastern bounding transform faults (Figures 3c and 3d). Following this pattern, the intensities of the CAMHs of both sectors decrease by ~9 A/m ~25 km from the eastern bounding transform faults (Figures 4c and 4d).

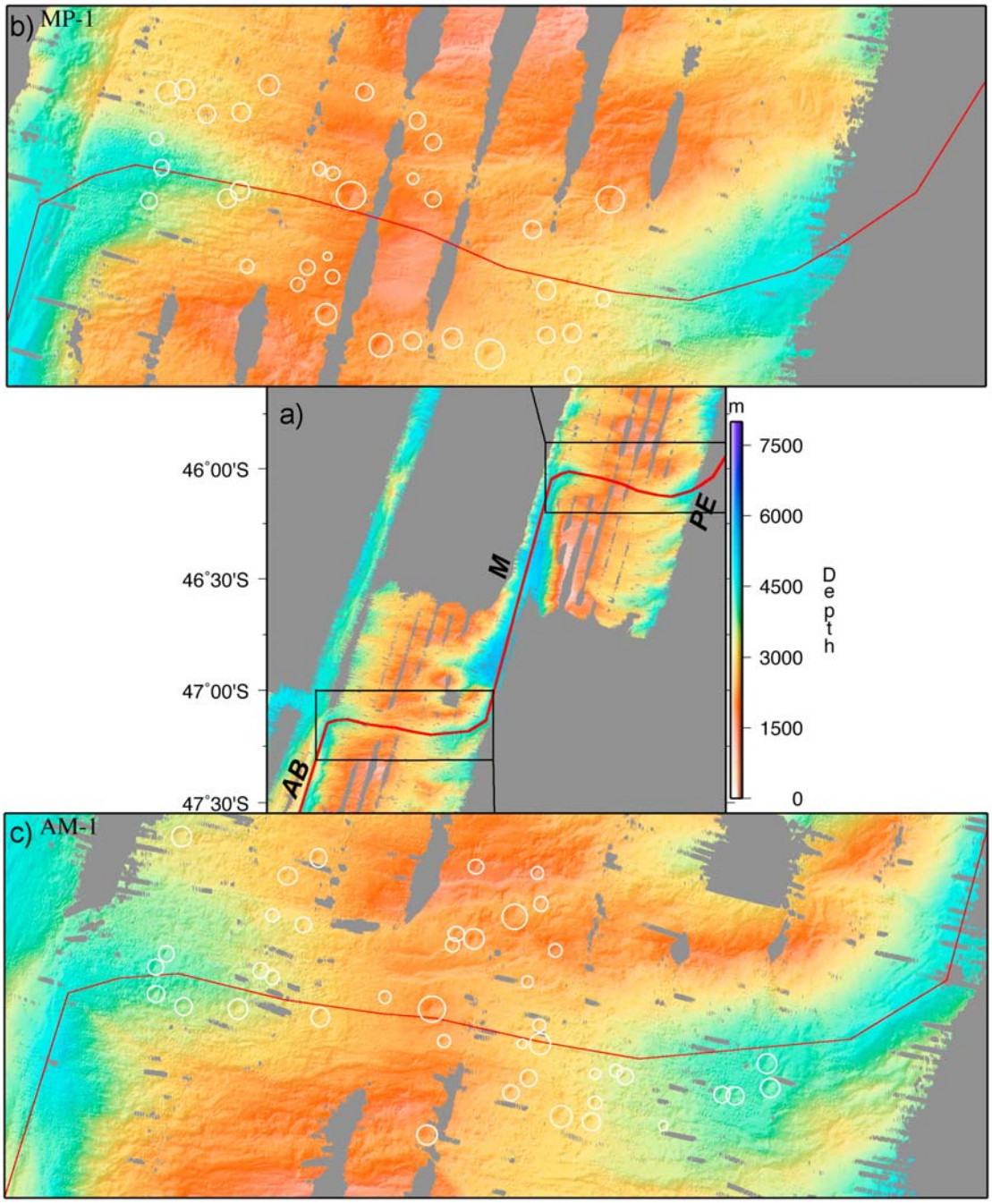


Figure 6. (a) High-resolution shipboard bathymetry (50 m grid interval) of the SWIR between 32°E and 35°E, survey area AP, showing the positive gradient in volcanic cone density from east to west in and around the rift valleys. Flat-topped mounds interpreted to be volcanic cones are circled in white. Illumination is from the south-southwest. Grey areas are between-track data gaps. Transform fault locations are labeled in Figure 6a as follows: AB, Andrew Bain; M, Marion; PE, Prince Edward. (b) Rift valley of segment MP-1. Note the abundance of volcanic cones and narrow volcanic ridge in the west, immediately adjacent to the Marion transform fault. In the east, shipboard bathymetric coverage does not extend all the way to the Prince Edward transform fault (located just off the eastern end of the plotted area; it connects to the ridge axis at the northeastern limit of the plate boundary plotted in red); however, the eastern limit of bathymetric coverage shows relatively fewer volcanic cones in and around the rift valley, at a greater distance from the Prince Edward transform fault. (c) Rift valley of segment AM-1, again showing a greater abundance of volcanic cones within a given distance of the Andrew Bain transform fault than within the same distance from the Marion transform fault.

4.4. Earthquake Locations

[26] Of the 27 relocated earthquake epicenters of *Engdahl et al.* [1998], 22 are located within or near the Andrew Bain, Marion, or Prince Edward transform domains (Figure 3a). Focal mechanisms in these locations indicate the expected dextral strike-slip faulting, except for a single normal faulting mechanism in the Marion transform domain. Five events are located within or near the rift valley between the Andrew Bain and Marion transform faults, including one normal faulting event.

5. Survey Area DA: 25.5°E–28°E

5.1. Morphology

5.1.1. Rift Valley

[27] Survey area DA is characterized by two overlapping rift valleys (Figure 7a). The western of the two (hereafter referred to as the western rift valley) is a low-relief (500 m), ~70 km long valley striking ~116°. At its western end, it begins to curve south ~20 km from its intersection with the northern end of the Du Toit transform fault. The valley is deepest in the nodal basin of the ridge-transform intersection (RTI), reaching a depth of ~5900 m (Figure 8a). It shoals by ~2500 m to the shallowest point of the rift valley, and then deepens by ~1100 m toward an elliptical basin in the east. The valley shoals and narrows east of this elliptical basin before disappearing. The mean depth of the western rift valley between the nodal basin in the west and the elliptical basin in the east is ~4500 m. No single distinct axial volcanic ridge (AVR) can be identified within the rift valley (Figure 9). Rather, a shallow, broad, low-relief swell topped by a series of small ridges and troughs lies in the center of the valley.

[28] The western rift valley overlaps with another rift valley to the south (the eastern rift valley) by ~22 km (Figure 7a). A ~1200 m high ridge sits between the overlapping valleys. The eastern rift valley lacks an arch-shaped profile; rather, it deepens from west to east (Figure 8a), reaching a maximum depth of ~6550 m at the Andrew Bain RTI. The eastern rift valley is ~65 km long, has a mean depth of 4850 m and no discernible AVR (Figure 9). The valley is roughly linear south of the valley overlap, striking ~92° before curving northward ~40 km from the Andrew Bain transform fault. The eastern rift valley deepens from west to east by ~1800 m (Figure 8a).

5.1.2. Seafloor Texture

[29] The seafloor texture of survey area DA is widely variable (Figure 9). The primary observation is the dearth of clearly identifiable volcanic cones anywhere in the area. Rather, the most abundant texture is that of hummocky volcanic terrain. The seafloor flanking the western rift valley is predominantly this hummocky terrain, both in the organized spreading-perpendicular abyssal hill fabric north of the rift valley (Figure 9b) and the Du Toit inside corner high (ICH) south of the valley (Figure 9c). The Du Toit ICH shows clear evidence of widespread faulting, with a number of scarps oriented subparallel to the western rift valley. Weak spreading-parallel lineaments can also been seen on the Du Toit inside corner high (the southwestern area of Figure 9c).

[30] North of the overlapping rift valleys, the seafloor shows some ridge-parallel abyssal hill fabric and hummocky terrain; however, this area is dominated by a circular, domal bathymetric high centered at 27°03′E, 52°24′S, which stands ~1 km above the surrounding seafloor (Figure 9). South of

Figure 7. (a) The 1 min gridded bathymetry of the SWIR between 25.5°E and 28°E, survey area DA. Bathymetric contour interval is 500 m. Black dots denote locations of earthquake solutions [*Engdahl et al.*, 1998], with focal mechanisms plotted where available. (b) The 1 min gridded mantle Bouguer anomaly. Shipboard bathymetry has been extended beyond the survey area with the GEBCO 1 min grid [*Fisher and Goodwille*, 1997] for MBA calculations. MBA contours are in black, interval is 5 mGal, and heavy black line indicates zero MBA contour. White contours are 1000 m bathymetric contours. (c) Reduced-to-the-pole magnetic anomalies. Positive amplitudes to the west-northwest. Purple symbols indicate the center of positive polarity intervals 1 (0–0.78 Ma, diamond), 2a (2.581–3.58 Ma, triangle), 3a (5.894–6.567 Ma, circle), and 4 (7.432–8.072 Ma, inverted triangle) [*Cande and Kent*, 1995]. (d) The 1 min gridded magnetization intensity. Magnetization contours are in black, interval is 1.25 A/m, and heavy black line indicates zero magnetization contour. White contours are 1000 m bathymetric contours. Purple symbols indicate magnetic anomaly picks as in Figure 7c. Red lines indicate the location of the plate boundary. Dashed red line indicates that the location of the plate boundary in this area is unknown. Transform fault locations are labeled in all plots as follows: DT, Du Toit; AB, Andrew Bain.

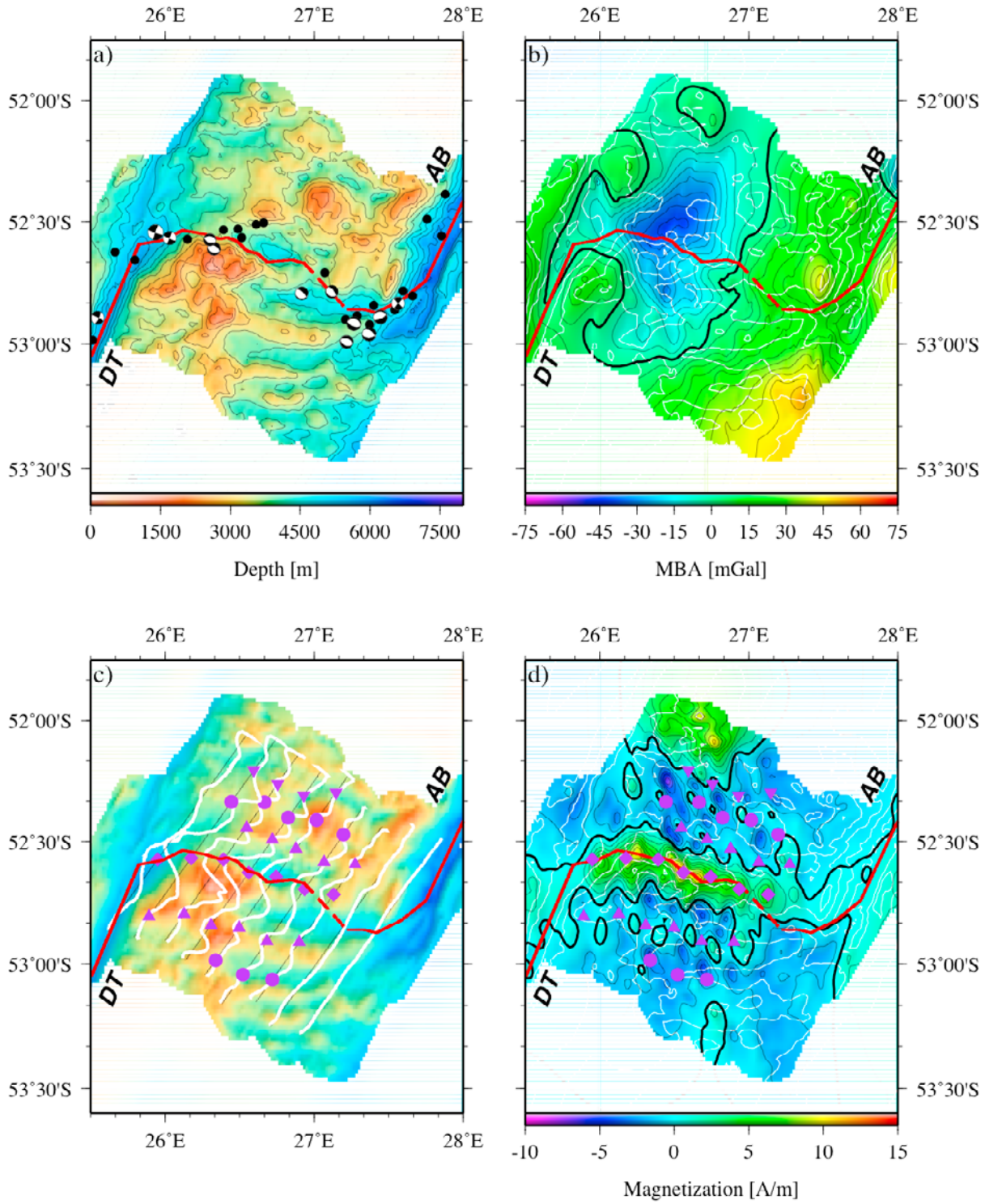


Figure 7

the valley overlap, the seafloor is covered by a series of long, broad, roughly parallel ridge-trough structures; the eastern rift valley is the northernmost trough in this configuration. This ridge-trough system is in stark contrast to the relatively gentle abyssal hill fabric north of the rift valley in the western area; the ridges have relief of up to 1 km relative to the intervening valleys. The ridges stand ~1500 m deeper than the northern Du Toit ICH, and taper and deepen to the east as they begin

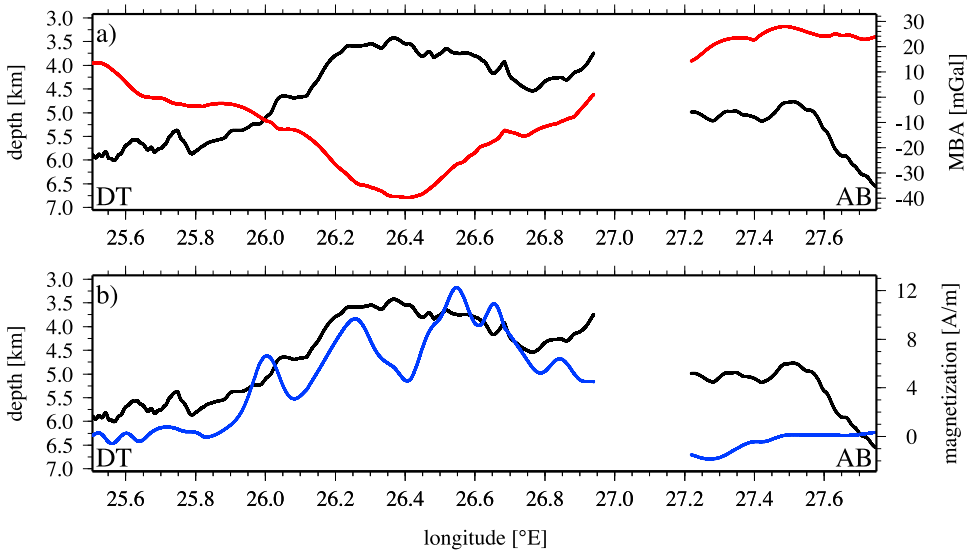


Figure 8. Along-axis bathymetry, MBA, and magnetization data for survey area DA. Fields are sampled along the plate boundary, plotted in red in Figure 7. Transform fault locations are labeled in both plots as follows: DT, Du Toit; AB, Andrew Bain. (a) Bathymetry (black) and MBA (red) between the Du Toit and Andrew Bain transform faults. (b) Bathymetry (black) and magnetization (blue) for the same area. Gaps in data in both plots indicate that the location of the plate boundary in this area is unknown.

to gently curve northward. At the western end of the ridge-trough system, the seafloor shows hummocky terrain similar to that of the Du Toit ICH; however, as the ridges deepen to the east, the terrain becomes very smooth, with little evidence of hummocky textures or fault scarps (Figure 9d). This smooth texture continues to the east all the way to the Andrew Bain fracture zone.

[31] Opposing the broad, smooth ridges across the eastern rift valley, on the inside corner of the Andrew Bain RTI, is a complex jumble of terrain. The seafloor is composed largely of rough, hummocky terrain similar to that of the Du Toit ICH (Figure 9e). However, the Andrew Bain inside corner shows no dominant directional fabric. A single ridge oriented parallel to the eastern rift valley cuts across the area, while other features are oriented at a variety of angles. Abundant scarps with short horizontal extents (~3 km), interpreted to mark faults, cut through the terrain with no preferred orientation. Contrary to the general disorganization of the area, the western flank of the lobate high centered at 27°10E, 52°43′S shows structured spreading-parallel lineaments (Figure 9f).

5.2. Mantle Bouguer Anomaly

[32] The MBA signature of survey area DA is dominated by a broad, irregularly shaped −40 mGal low centered slightly to the north of the western rift valley (Figure 7b). The MBA increases by ~53 mGal to the west along the rift valley. It increases almost monotonically eastward from the low, reaching a positive maximum of ~28 mGal near the eastern end of the northernmost broad ridge south of the eastern rift valley (Figure 8a). This rift valley maximum, however, is low relative to the off-axis MBA amplitudes of the eastern section, which are up to 20 mGal higher (Figure 7b).

5.3. Magnetization and Magnetic Anomalies

[33] The magnetic anomalies and crustal magnetization of survey area DA show a clear elongated central magnetic anomaly/CAMH over the southern flank of the western rift valley (Figures 7c and 7d). The central magnetic anomaly/CAMH extends the full length of the western rift valley, along the ridge between the overlapping valleys, and over the lobate spreading-parallel-lineated high north of the center of the eastern rift valley. Intensity variations within the CAMH are broadly arch shaped. They have a maximum near the elliptical basin at the eastern end of the western rift valley, and weaken by ~12 A/m to both the west and east (Figure 8b). However, the overall along-axis magnetization and magnetic anomaly distributions are asymmetric. While the CAMH and central magnetic anomaly are clearly visible within the western section of the survey area, up to within ~10 km of the Du Toit

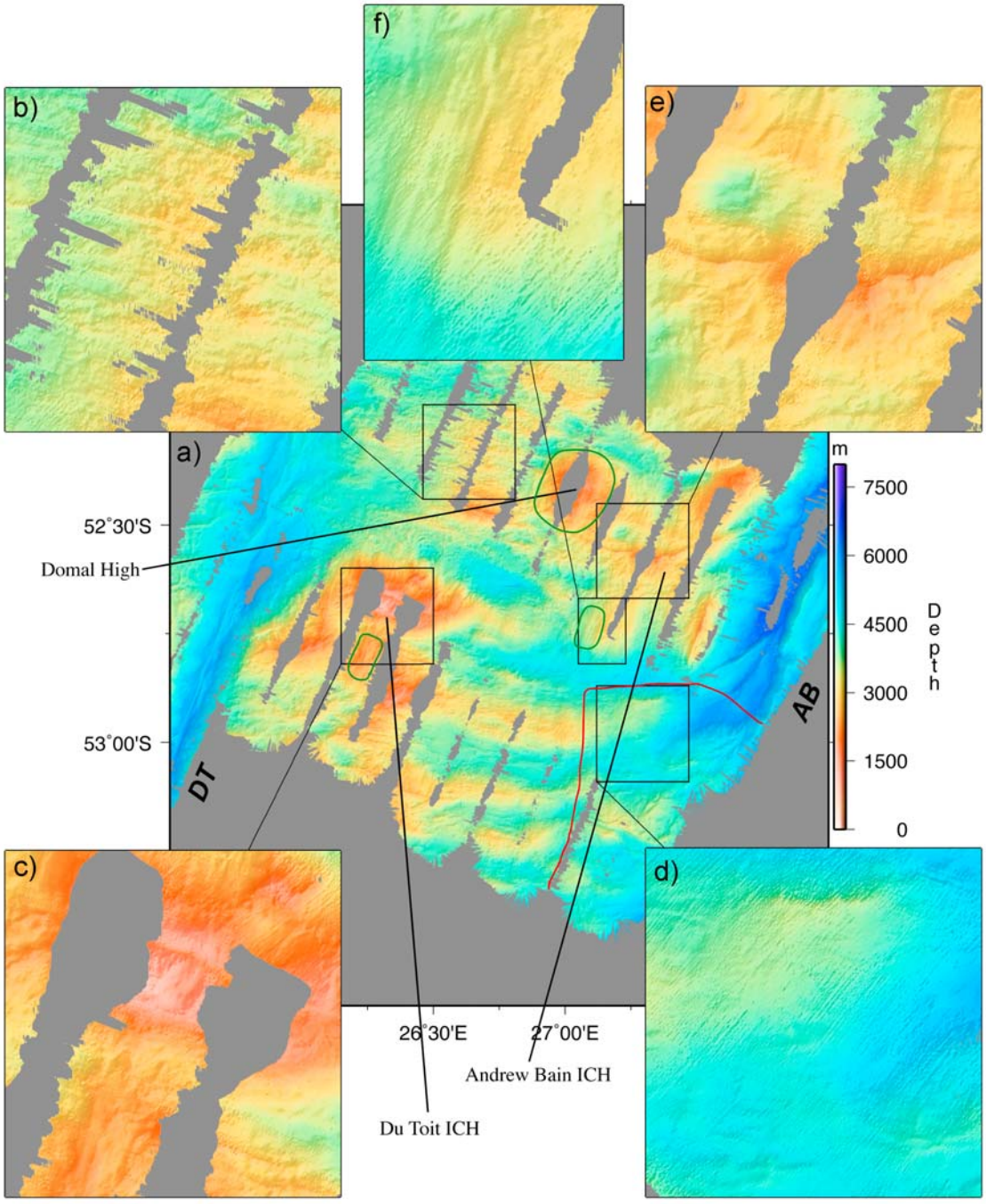


Figure 9. (a) High-resolution shipboard bathymetry (50 m grid interval) of the SWIR between 25.5°E and 28°E. Illumination is from the west-northwest. Grey areas are between-track data gaps. Transform fault locations are labeled in Figure 9a as follows: DT, Du Toit; AB, Andrew Bain. Red line delineates areas interpreted to be smooth nonvolcanic seafloor. Green lines indicate areas showing characteristics of corrugated seafloor. (b) Abyssal hill fabric on the northern flank of the western rift valley. (c) Hummocky volcanic terrain on the Du Toit inside corner high. Southwestern area shows weak spreading-parallel lineations. (d) Smooth, broad ridge with no evidence of volcanic cones or fault scarps south of the eastern rift valley. (e) Hummocky volcanic terrain on the Andrew Bain inside corner. (f) Lobate high on the northern flank of the eastern rift valley showing clear spreading-parallel lineaments on its western flank.

transform fault, they decay to the east, disappearing entirely ~35 km from the Andrew Bain transform fault (Figures 7c and 7d). Similarly, while weak magnetic lineations persist off axis near the Du Toit fracture zone, they do not exist in the eastern section.

5.4. Earthquake Locations

[34] A total of 32 relocated earthquake epicenters lie within survey area DA [*Engdahl et al.*, 1998] (Figure 7a). Eleven of these are found within the transform domains bounding the ridge axis, four in the Du Toit and seven in the Andrew Bain. The remainder are clustered around the two rift valleys, and follow their overlap and possible offset. Focal mechanisms indicate normal faulting within the rift valleys and dextral strike-slip faulting in the transform domains, as would be expected. Eleven earthquake epicenters lie within or near the eastern rift valley. Eight of these are clustered around a deep basin within the rift valley at 27°17′E, 52°52′S. Three lie well to the west in the central part of the valley. Ten events are located near the western rift valley, including two strike-slip mechanisms near the nodal basin of the Andrew Bain RTI.

6. Ridge Segmentation and Plate Boundary Location

[35] Our observations allow us to define three segments between 25.5°E and 35°E on the SWIR. Two are located in survey area AP, one between the Andrew Bain and Marion transform faults, the other between the Marion and Prince Edward transform faults. These segments are defined primarily on a morphological basis; they both have arch-shaped along-axis bathymetric profiles uninterrupted by higher-order offsets and are thus straightforward first-order segments [*Macdonald et al.*, 1988; *Grindlay et al.*, 1991]. They both have rift valleys, partially or completely filled by a volcanic edifice, deep bull's-eye MBA lows, and high-magnetization amplitudes. We follow the naming convention of *Hosford et al.* [2003] and *Baines et al.* [2007] and denote these segments AM-1 and MP-1. Since the AVRs within the rift valleys of these two segments are obscured, we place the plate boundary at the line of greatest depth (Figure 3).

[36] Between the Du Toit and Andrew Bain transforms faults, the segmentation is not as easily defined, as the plate boundary cannot be located at every point. In the western section, to achieve the best agreement among the morphology, the magnetization, and the earthquake locations, we place the plate boundary on the southern wall of the western rift valley, following the central magnetization high (Figure 7). In the eastern section, the magnetization provides little control; as such, we locate the plate boundary along the deepest part of the eastern rift valley, in agreement with the earthquake locations. Between these two sections, the location of the plate boundary is unclear (dashed line in Figure 7).

[37] If a ridge axis offset within survey area DA does indeed exist, then there would clearly be two individual segments by the basic definition of ridge segmentation. The earthquake locations would support this definition, as they appear to step to the right, following the locations of the two rift valleys (Figure 7a). However, we cannot definitively locate a clear offset in the morphology. The magnetization and magnetic anomalies show no evidence of an offset in the central magnetic anomaly/magnetization high (Figures 7c and 7d). The gravity data show a single bull's-eye MBA low, evidence of a single zone of melt supply and/or mantle upwelling (Figure 7b). Hence, while rift valley morphology and earthquake locations support the designation of two distinct segments, the magnetic and gravity data support the designation of only one. As section 7 will show, our analysis does not depend on a possible offset of the ridge axis. Thus, we will utilize a single gravimetric segment, DA-1, for the remainder of this study.

7. Interpretation of Observations

7.1. Definitions and Cautions

[38] For the sake of clarity, we introduce some terminology that distinguishes between the various factors that influence the amount of melt that ridge segments receive. The terms "melt supply" and "melt production" will refer to the volume of melt produced by partial melting of the upwelling mantle, with enhanced upwelling producing more melt. "Melt focusing" refers to the lateral migration of melt within or between individual segments, away from discontinuities and/or oblique segments and toward orthogonal segment centers. "Melt delivery" refers to the amount of melt emplaced within a given ridge segment, and is thus a sum of melt supply, melt focusing, and any other processes that influence shallow melt emplacement (e.g., crustal magma plumbing). Variable regional melt supply produces variations in regional axial depth and basalt sodium content [*Klein and Langmuir*,

1987; *Cannat et al.*, 2008]. Melt focusing causes melt delivery to and within individual segments to vary [*Magde et al.*, 1997; *Magde and Sparks*, 1997; *Cannat et al.*, 2003, 2008]. This produces segment-scale and intrasegment variation in crustal and extrusive volcanic layer thickness.

[39] In the following analysis, we use gravimetric and magnetic data in our investigation of segment-scale and intrasegment melt delivery variations. However, caution must be taken with this approach for a variety of reasons. MBA amplitudes include signals from crustal thickness, crustal density, and mantle density; as we lack seismic crustal thickness data, our gravity data are unconstrained. Similarly, our magnetization data cannot distinguish between intensity variations and lateral variations in the thickness of the magnetic source layer.

7.2. Seafloor Texture as an Indicator of Melt Supply and Delivery

[40] Fortunately, seafloor texture is a strong indicator of melt delivery [*Cannat et al.*, 2006]. On the SWIR, melt delivery variations produce three different types of seafloor [*Cannat et al.*, 2006]. The first type is MAR-like volcanic seafloor, which occurs in times and/or locations of relatively high melt delivery. Magmatic seafloor is characterized by numerous volcanic cones, hummocky terrain, and fault scarps ~50–500 m high bounding ridge-parallel abyssal hills.

[41] The second type of seafloor is unique to ultraslow spreading ridges: smooth seafloor, which occurs at times and or/locations of low melt delivery. Smooth seafloor is predominantly found at oblique sections of the SWIR. These sections are typically marked by an axial trough with high MBA amplitudes, low magnetization intensity, and no evidence of volcanic edifices, flanked by broad, smooth ridges [*Dick et al.*, 2003; *Sauter et al.*, 2004b; *Cannat et al.*, 2006]. Dredging of smooth seafloor reveals compositions of primarily mantle-derived peridotite, with thin and/or scattered basalts and gabbros [*Dick et al.*, 2003; *Seyler et al.*, 2003].

[42] The third type, corrugated seafloor, occurs very infrequently. Corrugated seafloor is characterized by dome-shaped features with spreading-parallel lineations <1 km wide and 30–100 m high [*Cannat et al.*, 2006]. This morphology has been interpreted to reflect the exposed footwall of a low-angle detachment fault [e.g., *Tucholke and Lin*, 1994]. While it was originally thought that corrugated seafloor reflects low melt supply [*Tucholke and Lin*, 1994], recovery of large volumes of gabbro in cores drilled into the domes [e.g., *Dick et al.*, 2000; *Blackman et al.*, 2006] and numerical experiments [*Tucholke et al.*, 2008] indicate that corrugated seafloor forms at times and/or locations with a narrow window of intermediate melt delivery.

7.3. Observations of Asymmetries in Melt Delivery and Lithospheric Thickness

[43] Our analysis of the seafloor texture of segments AM-1 and MP-1 has revealed exclusively volcanic terrain, including hummocky terrain and numerous circular flat-topped mounds, which we interpret as volcanic cones (Figures 5 and 6). Our magnetic analysis shows that magnetization intensity decreases from segment centers to segment ends. This is a typical observation of SWIR segments, and has been attributed to a reduction in the frequency of volcanic eruptions away from segment centers, which thins the extrusive volcanic layer and thus the magnetic source layer [*Sauter et al.*, 2004a]. The westward skew of magnetization intensity thus means that the magnetic source layer is relatively thick on the western ends of the segments. This conclusion is supported by an along-axis gradient in the observed density of volcanic cones in and around the rift valleys of segments AM-1 and MP-1, with more volcanic cones near the western bounding transform faults than the eastern (Figure 6). Similarly, asymmetries in MBA amplitudes show that the western ends of segments AM-1 and MP-1 have a mass deficit relative to their eastern ends.

[44] Segment DA-1 also shows a very prominent asymmetry in seafloor textures. The three seafloor textures described earlier [*Cannat et al.*, 2006] are all present within segment DA-1. The western end is composed almost exclusively of volcanic seafloor, both in the abyssal hill fabric north (Figure 9b) of the ridge axis and the Du Toit ICH south of the axis (Figure 9c). We interpret the broad ridges south of the axis on the eastern end of the segment as smooth seafloor; they lack any evidence of volcanic cones or other volcanic terrain (Figure 9d). This smooth seafloor is opposed by volcanic seafloor north of the axis (Figure 9e). In the center of the segment, the ridges south of the axis have an increasingly volcanic texture from east to west. Three areas have characteristics of corrugated seafloor. The western flank of the lobate high centered at 27°10′E, 52°43′S shows clear spreading-parallel corrugations (Figure 9f); one small area of possible corrugated seafloor is also observed on the Du Toit

ICH (the southwestern area of Figure 9c). The large high centered at 27°04′E, 52°26′S has the characteristic domal shape of corrugated seafloor; however, the flanks of the dome show no evidence of corrugations and a bathymetric data gap prevents us from observing the texture on the summit. The segment thus shows an east-west gradient in seafloor texture, with nearly equal volumes of smooth and volcanic seafloor on the eastern end of the segment transitioning to almost entirely volcanic seafloor on the western end.

[45] MBA amplitude variations parallel the gradient in seafloor texture within segment DA-1, with high amplitudes in the east where smooth seafloor dominates and low amplitudes in the west where volcanic seafloor prevails (Figures 7b and 8a). Caution must be taken in the interpretation of the MBA. The assumption that MBA variations can largely be attributed to crustal thickness variations, frequently utilized for MAR segments, does not apply for the case of segment DA-1, as the prevalence of nonvolcanic seafloor indicates that lateral density variations in both the crust and mantle certainly contribute to the MBA signal. Similarly, the along-axis variation in magnetic anomaly amplitude and magnetization intensity (Figures 7c and 8b) undoubtedly contains signal from both variable source layer thickness and intensity, as highly variable seafloor textures, and thus compositions, and pervasive faulting will create disorganized and unpredictable source layer properties.

[46] Another striking asymmetry common to all three segments is that of rift valley curvature. At their western ends, the rift valleys of segments AM-1 and MP-1 intersect the bounding transform faults nearly orthogonally (Figure 5). Abyssal hills curve southward only within 5–7 km of the fracture zones. At their eastern ends, the rift valleys begin curving north just east of the shallowest points of the segments, 20–30 km from the bounding transform faults. The western rift valley of segment DA-1 begins to curve south ~20 km from the Du Toit transform fault, while the eastern rift valley begins to curve north ~40 km from the Andrew Bain transform fault (Figure 9).

[47] Our observations of the west-east asymmetries in these three segments indicate three effects: (1) magmatic activity is higher in the west, producing greater volumes of volcanic seafloor textures, thicker extrusive volcanic layers and/or higher magnetization, and higher magnetic anomaly amplitudes; (2) the lithospheric welds controlling rift valley curvature are weak in the west relative to the east; and (3) relative mass deficits exist in the west, as reflected in lower MBA amplitudes there. The asymmetries of volcanic seafloor and extrusive volcanic layer thickness may be most easily explained by intrasegment variations in melt delivery, i.e., a greater volume of melt emplaced at shallow depths at the western end of the segments than at the eastern ends. The asymmetries in rift valley curvature may be explained by thin subaxial lithosphere and thus weaker lithospheric welds beneath the western ends of the segments. Relative mass deficits at the western ends of the segments may be explained by a combination of the above mechanisms: low MBA amplitudes could result from both thicker crust (i.e., greater melt delivery) and thin subaxial lithosphere (i.e., greater volumes of hot, relatively low density asthenopheric mantle at shallow depths). That all three segments show broadly similar asymmetries suggests that they may have a single common mechanism. However, obvious differences do exist, most prominently the presence of nonvolcanic seafloor within segment DA-1 versus the lack thereof within segments AM-1 and MP-1. In section 8, we will investigate possible explanations for the observed asymmetries, each of them involving relative motion between the spreading ridge and the underlying mantle.

8. Models of Asymmetric Melt Delivery

8.1. Ridge Migration

[48] The first mechanism investigated involves migration of the spreading ridge in the hot spot reference frame. This migration results in an increase in melt supply and melt delivery, reflected in shallower depths, at leading ridge segments [*Carbotte et al.*, 2004]. It is possible, then, that westward migration of the SWIR over the underlying mantle could produce asymmetric mantle upwelling under, and increased melt delivery to, the western ends of segments DA-1, AM-1, and MP-1. To test this hypothesis, we calculate the migration of the SWIR at several points between 14°E and 42°E using the absolute plate motion model HS3-Nuvel1a [*Gripp and Gordon*, 2002] (Figure 10). The direction of motion of the SWIR in this region is predominantly south. As such, ridge migration cannot be responsible for our observed asymmetries.

8.2. Subaxial Asthenospheric Flow: Segment DA-1

[49] A broad along-axis asthenospheric flow, produced by gradients in mantle temperature, has been

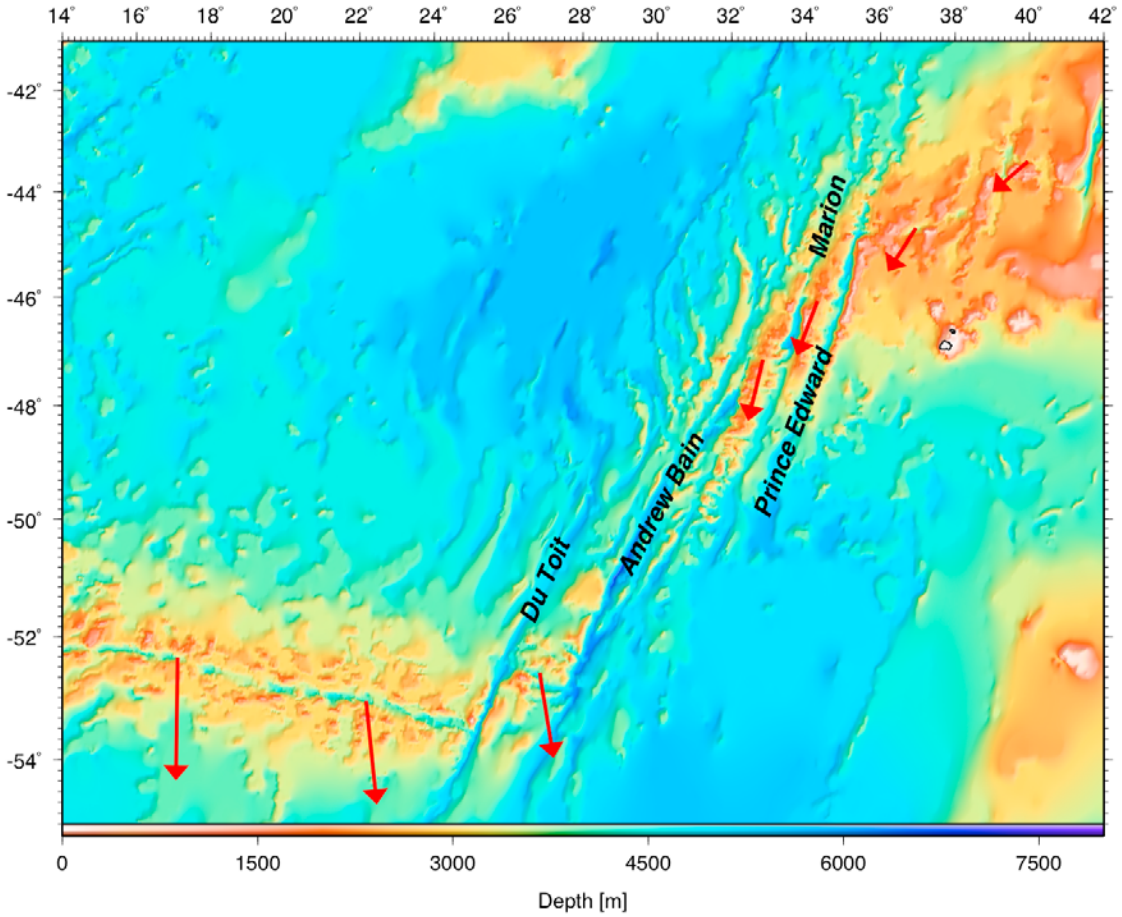


Figure 10. The 1 min GEBCO bathymetry of the SWIR between 14°E and 42°E [*Fisher and Goodwille*, 1997]. Red arrows indicate vectors of ridge migration in the hot spot reference frame, calculated from the absolute plate motion model HS3-Nuvel1a [*Gripp and Gordon*, 2002]. Arrow lengths are proportional to rate of migration; migration for segment AM-1 is 7 mm/yr.

invoked to explain along-axis asymmetries in axial depths and MBA amplitudes observed between 98°E and 112°E on the Southeast Indian Ridge (SEIR) [*West and Sempéré*, 1998]. This mechanism involves flow entering the upstream end of a ridge segment from beneath the older, thicker adjacent lithosphere [see *West and Sempéré*, 1998, Figure 6]. Similar asymmetries have been observed within the 15.5°E–25°E supersegment of the SWIR [*Grindlay et al.*, 1998]. Relatively shallow depths and low MBA values on the western end of the supersegment have been ascribed to enhanced mantle upwelling, likely due to hotter mantle temperatures underneath this part of the ridge.

[50] Eastward subaxial flow could also explain weakening of the lithospheric weld responsible for rift valley curvature on the upstream segment end. Enhanced upstream mantle upwelling would advect heat into this area, warming and thinning the subaxial lithosphere, thus reducing the strength of the lithospheric weld. This model could thus potentially explain the asymmetries observed in segment DA-1; enhanced mantle upwelling and melting would then be focused on the western, upstream end of the segment, producing axial depth and MBA amplitude patterns mirroring those observed in the 15.5°E–25°E SWIR supersegment and the 98°E–112°E SEIR region, as well as the observed stronger magnetization intensity and weaker lithospheric weld in the west. In principle, segment DA-1 could be on the distal end of the same mantle upwelling asymmetry proposed by *Grindlay et al.* [1998] to explain their along-axis variations in axial depth and MBA. However, eastward subaxial flow model does not explain the presence of nonvolcanic seafloor and low melt delivery at the eastern end of segment DA-1, a feature that does not appear at the eastern ends of segments within

the 15.5°E–25°E SWIR supersegment nor the 98°E–112°E region of the SEIR.

8.3. Subaxial Asthenospheric Flow: Segments AM-1 and MP-1

8.3.1. Eastward Flow?

[51] Segments AM-1 and MP-1 lie ~250 and ~330 km away from Marion Island, the current seafloor expression of the Marion hot spot (Figure 1, inset). Seismic tomography has revealed the presence of a regional negative shear wave velocity anomaly at 75 km depth in the vicinity of the hot spot, which has been interpreted to reflect a hotter mantle in this area [*Debayle et al.*, 2005; *Sauter et al.*, 2009]. Anomalously shallow bathymetry [*Sauter et al.*, 2009] and low regional MBA amplitudes [*Georgen et al.*, 2001] between the Andrew Bain and Discovery II transform faults (~32°E to 41.75°E) have been interpreted to reflect regional-scale thick crust due to the presence of the Marion hot spot [*Georgen et al.*, 2001] and thus increased regional melt supply along this section of the ridge [*Cannat et al.*, 2008].

[52] If segments AM-1 and MP-1 are indeed within the sphere of influence of the Marion hot spot, a subaxial asthenospheric flow could be explained via either channelized flow along the ridge [e.g., *Vogt and Johnson*, 1975; *Georgen and Lin*, 2003], or diffuse radial flow outward from the hot spot [e.g., *Ribe et al.*, 1995; *Georgen et al.*, 2001]. We cannot definitively discount the possibility of an eastward mantle flow. However, due to the location and orientation of the segments with respect to the Marion hot spot, either channelized subaxial flow or diffuse radial flow would far more likely be directed to the west, with enhanced melt delivery on the downstream rather than the upstream ends of the segments. As such, it would appear that the asymmetries observed on either side of the Andrew Bain result from different mechanisms.

8.3.2. Influence of the Marion Hot Spot

[53] Before we investigate how the Marion hot spot could produce the observed asymmetries, we must first show that segments AM-1 and MP-1 are influenced by the hot spot. Unfortunately, the limited dredge sampling within these two segments (green dots in Figure 3a [*Mahoney et al.*, 1992]) have not conclusively revealed the presence or lack of Marion basalts at the ridge; Marion basalts have a geochemical signature more similar to that of MORB than that of incompatible-rich ocean island basalts (OIB) [*Meyzen et al.*, 2005]. However, we may utilize our bathymetric and gravimetric observations to infer that segments AM-1 and MP-1 receive a high supply of melt, as they should if they are influenced by the hot spot. To demonstrate that these two segments have high melt supply, we compare various melt supply indicators to those of other segments of the SWIR (Table 1). Based on regional axial depth and basalt sodium content, *Cannat et al.* [2008] have placed the segments in Table 1 other than AM-1 and MP-1 within various melt supply regions: segment 27 is within a high melt supply region; the 15.5°E–25°E supersegment is a moderate melt supply region, as is the region containing segments 20–22. Segments 11 and 14 are within low melt supply regions. Segments AM-1 and MP-1 are on the western edge of a high melt supply region which is bounded by the Prince Edward and Discovery II transform faults.

[54] We compare segment length versus along-axis relief, axial relief versus along-axis MBA variation, segment length versus along-axis MBA variation, and mean axial depth versus along-axis MBA variation for the segments listed in Table 1 (Figure 11). Weak correlations between length and axial relief, and length and MBA amplitude, for the segments in the moderate melt supply 15.5°E–25°E supersegment have been attributed to weak shallow melt focusing [*Grindlay et al.*, 1998]. For segments 20–22, higher MBA amplitudes for similar length, axial relief, and regional melt supply to the 15.5°E–25°E segments reflects a higher degree of melt focusing, most reasonably due to larger bounding offsets between segments and thus thicker lithosphere at the segment ends [*Sauter et al.*, 2001]. The high relief and MBA amplitude of segment 27 has been attributed to high melt supply produced by a melting anomaly carried to the SWIR from the Crozet hot spot [*Sauter et al.*, 2009]. This conclusion is supported by the large abyssal hills observed at this segment; abyssal hill relief has recently been correlated with crustal thickness, with greater relief abyssal hills occurring in segments with greater crustal thickness and melt supply [*Mendel et al.*, 2003]. High relief and high MBA amplitudes at segments 14 and 11, coupled with relatively long segment lengths, have been attributed to strong shallow melt focusing; this focusing explains why these segments have similar relief and MBA amplitudes to segment 27 despite having low regional melt supply [*Cannat et al.*, 1999].

Table 1. Segment Length, Mean Axial Depth, Along-Axis Relief, Across-Axis Relief, Along-Axis MBA Variation, and Regional Basalt Sodium Content for Seven Areas Along the SWIR[a]

Location	Segment Length (km)	Mean Axial Depth (m)	Along-Axis Relief (m)	Across-Axis (Abyssal Hill) Relief (m)	MBA Variation (mGal)	Regional Basalt $Na_{8.0}$ (wt %)
15.5°E–25°E supersegment	21.5–77.5	3747	640–1180	200–600	7.5–31	~3.25
DA-1w	70	4500	2500	-	53	-
AM-1	85	3650	2100	500–800	35	−(2.71)
MP-1	85	3200	2900	500–1000	48	−(2.71)
Segment 27	85	2700	1900	500–900	51	2.61
Segments 20–22	40–45	4200	900–1300	100–350	42–33	3.03
Segment 14	65.1	4742	2352	-	40.4	3.89
Segment 11	60.4	4542	2672	-	53.1	3.72

[a]Listed from west to east: the 15.5°E–25°E orthogonal supersegment [*Grindlay et al.*, 1998], the western rift valley of segment DA-1 (current study, denoted as DA-1w), segments AM-1 and MP-1 (current study), segment 27 (50.47°E) [*Sauter et al.*, 2001; *Mendel et al.*, 2003], segments 20–22 (54.1°E–56.67°E) [*Sauter et al.*, 2001; *Mendel et al.*, 2003], and segments 14 and 11 (~61.4°E and 63.9°E, respectively) [*Cannat et al.*, 1999]. Regional basalt sodium content values from all regions are from *Cannat et al.* [2008], except for the 15.5°E–25°E supersegment [*Standish et al.*, 2008]. Sodium contents in parentheses for segments AM-1 and MP-1 indicate values published for the adjacent melt supply region [*Cannat et al.*, 2008]; no values for these specific segments have been published. Across-axis relief values for the western rift valley of DA-1 have not been calculated because the Du Toit inside corner high produces very asymmetric topography.

[55] Segments AM-1 and MP-1 have a greater similarity to segments 11, 14, and 27 than they have to either the 15.5°E–25°E segments or segments 20–22 (Figures 11a–11c), meaning that they have a high degree of melt delivery. However, if we are to suggest a Marion hot spot influence, we must demonstrate that segments AM-1 and MP-1 have high melt supply, regardless of the amount of melt focusing that occurs. The axial depths of segments AM-1 and MP-1 are considerably shallower than those of the low melt supply segments 11 and 14 (Figure 11d). Also, the abyssal hills on the flanks of segments AM-1 and MP-1 are similar in size to those of high melt supply segment 27 (Table 1). Given these observations, the inferred relation of regional axial depth and melt supply, and the location of segments AM-1 and MP-1 on the edge of a high melt supply region [*Cannat et al.*, 2008], we conclude that the high relief and MBA amplitudes of segments AM-1 and MP-1 result predominantly from high melt supply rather than strong melt focusing.

8.3.3. Flow From the Marion Hot Spot

[56] It is not known whether Marion hot spot flow to the ridge is channelized or diffuse/radial. However, the observation that the depth and gravity anomalies associated with the Marion hot spot are confined between the Andrew Bain and Discovery II transforms suggest that hot spot material is channeled along the ridge. Numerical modeling suggests that hot spot material delivered to the SWIR near the Eric Simpson Fracture Zone (~40°E) could successfully negotiate its way along the ridge to segments MP-1 and AM-1 before stagnating near the Andrew Bain transform fault [*Georgen and Lin*, 2003].

[57] Channelized subaxial asthenospheric flow along a ridge from a hot spot has been previously investigated by *Vogt and Johnson* [1975]. In their model, partial melts are entrained in a shallow pipelike asthenospheric flow pool against the thick lithosphere abutting the end of the ridge segment across the discontinuity. The pooled melts then propagate upward through the ridge axis, producing thicker crust and constructional volcanic features on the downstream end of the segment (see Figure 1 [*Vogt and Johnson*, 1975]).

[58] This model can explain the observed asymmetries of segments AM-1 and MP-1. Melt pooling against the Andrew Bain and Marion transform faults, on the downstream end of a possible westward channelized flow in the asthenosphere under segments AM-1 and MP-1, respectively, could account for thicker crust and a thicker extrusive volcanic layer on the western ends of the segments. The excess melt could also possibly explain the presence of the narrow ridge just east of the Marion transform fault in segment MP-1 (Figure 6b); this ridge resembles the constructional volcanic ridges discussed by *Vogt and Johnson* [1975]. The interaction of hot channelized flow from the Marion hot spot with the downward sloping lithosphere at the downstream end of the segments could also serve to heat and thin this lithosphere, reducing the strength of the lithospheric weld.

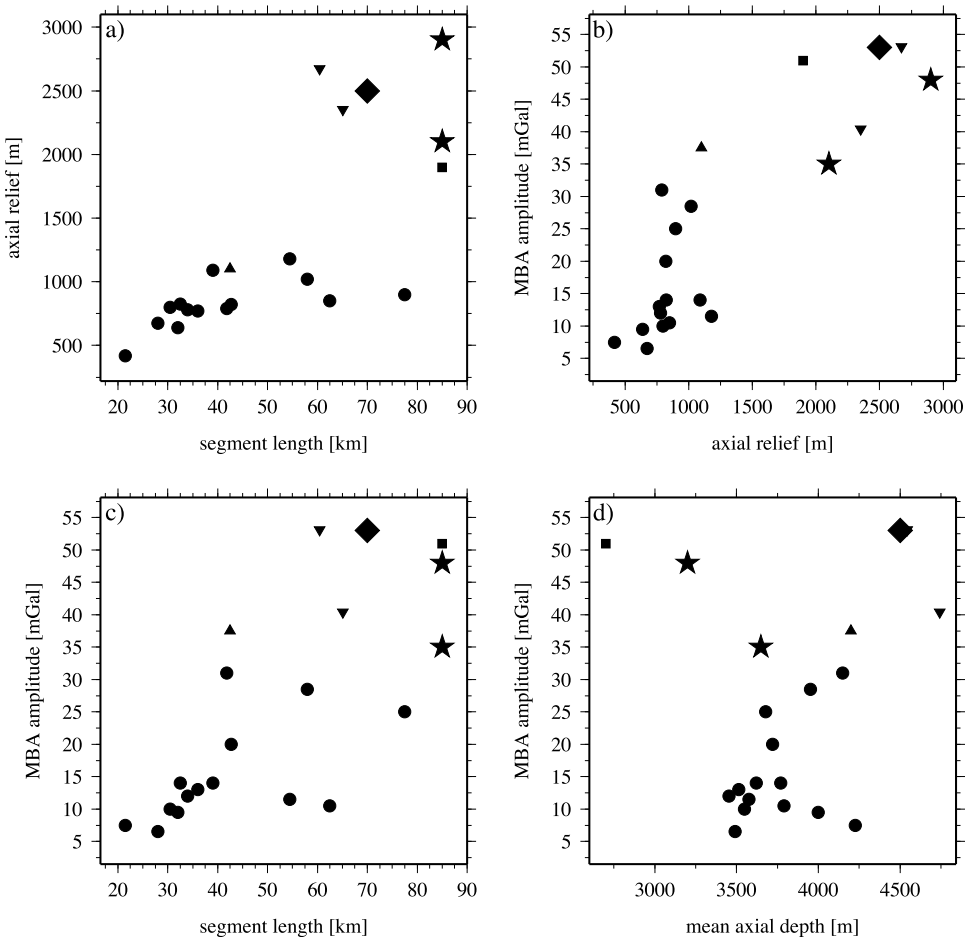


Figure 11. (a) Segment length versus axial relief, (b) axial relief versus MBA amplitude, (c) segment length versus MBA amplitude, and (d) mean axial depth versus MBA amplitude for seven areas along the SWIR, listed from west to east: the 15.5°E–25°E supersegment containing 14 individual accretionary segments [*Grindlay et al.*, 1998] (circles), the western rift valley of segment DA-1 (current study, diamond), segments AM-1 and MP-1 (current study, stars), segment 27 (50.47°E) [*Sauter et al.*, 2001; *Mendel et al.*, 2003] (square), segments 20–22 (54.1°E–56.67°E) (*Sauter et al.* [2001] (triangle, one record for all three segments) and *Mendel et al.* [2003]), and segments 14 and 11 (~61.4°E and 63.9°E, respectively) [*Cannat et al.*, 1999] (inverted triangles). Values plotted for segments 20–22 represent the central values of the ranges listed in Table 1.

[59] *Georgen and Lin* [2003] have suggested that Marion hot spot material may enter the SWIR somewhere near the Eric Simpson fracture zone. If this is the case, channelized subaxial flow would proceed in both directions along the ridge; as such, we would expect to see similar enhanced melt delivery on the downstream side of both the Prince Edward and Discovery II transforms. However, no high-resolution shipboard data for this region have been published. As such, we lack the ability to assess seafloor texture, rift valley curvature, and magnetic anomaly/magnetization variations within the region as we have for our survey area. MBAs, potentially calculated from the GEBCO bathymetry data [*Fisher and Goodwille*, 1997] and gravity data from satellite altimetry [*Sandwell and Smith*, 2009] cannot constrain lithospheric thickness and melt delivery variations by themselves.

8.4. Segment DA-1: Influence of the Long-Offset Andrew Bain Transform Fault

[60] Smooth nonvolcanic seafloor is ordinarily found within oblique segments of the SWIR. While we cannot discount the effects of innate ridge obliquity on melt delivery within segment DA-1, there is a simple mechanism that could account for thick lithosphere, low melt delivery, and even ridge obliquity at the eastern end of the segment. The Andrew Bain transform domain is composed of a 450 km long southern transform valley connected to a 100 km long northern transform valley by a

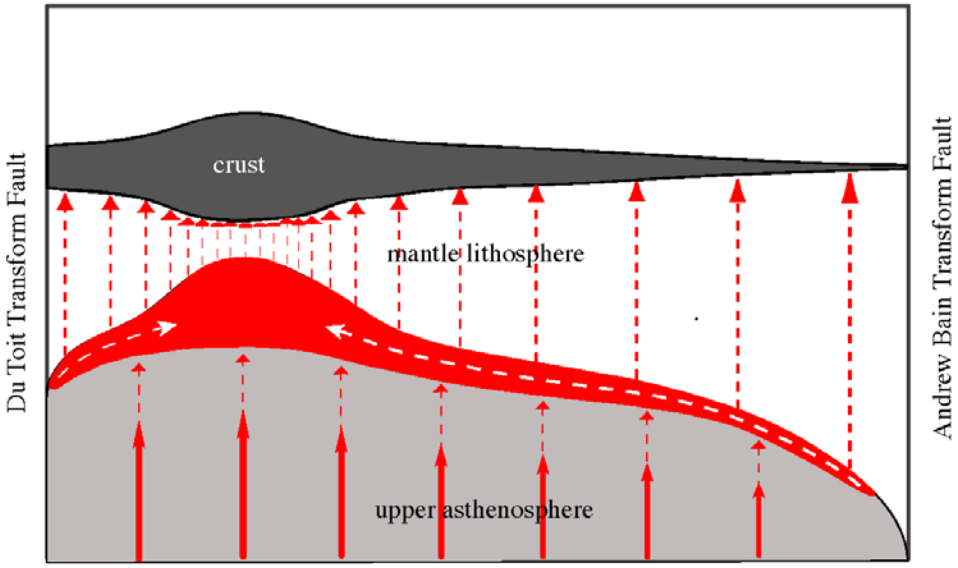


Figure 12. Cartoon (not to scale) showing our proposed mechanism for the along-axis distribution of melt and resulting observed asymmetries, which are strongly controlled by the transform edge effect. Passively upwelling mantle material (solid red arrows) undergoes partial melting and releases melt (dashed red arrows) to the top of the asthenosphere. This melt is then focused away from the bounding transform faults, up the sloping base of the lithosphere (dashed white arrows) [*Magde and Sparks*, 1997]. However, melt production is suppressed and melt focusing is enhanced by the strong cooling and thickening of the lithosphere towards the long-offset Andrew Bain transform to the east. The majority of what little melt is produced in the mantle near the Andrew Bain is focused toward the west or trapped in the thick lithosphere; very limited melt reaches shallow depths to create a crust primarily composed of a thin basaltic cap. Melt delivery increases to the west through westward melt focusing and increased melt production (along-axis density of dashed red arrows in the lithosphere indicates the relative amount of melt released from the upper asthenosphere that becomes crust).

series of extensional relay basins [*Sclater et al.*, 2005]. Using the southern transform valley length, a half spreading rate of 9 mm/yr (to get a minimum estimate of the age offset), and the relation for lithospheric thickness as a function of age of *Parker and Oldenburg* [1973],

$$Z(t) = 9.4\ t^{1/2}\ \text{km},$$

the Andrew Bain juxtaposes ~66 km thick lithosphere against the eastern end of DA-1. This extremely thick, cold lithosphere strongly cools and thickens the subaxial lithosphere of segment DA-1. At the northern end of the Andrew Bain, significantly thinner lithosphere (~31 km) abuts segment AM-1; the cooling effects of this lithosphere are not only weaker, but also mitigated by the along-axis asthenospheric flow from the Marion hot spot.

[61] Thus, we envision that the low melt delivery and nonvolcanic seafloor at the eastern end of segment DA-1 are effects of extremely thick subaxial lithosphere due to the Andrew Bain transform fault (Figure 12). In this model, the cooling of the subaxial lithosphere at the eastern end of segment DA-1 by the cold, thick lithosphere abutting it strongly suppresses melt production. The majority of what little melt is produced under the eastern end of segment DA-1 flows westward along the sloping base of the lithosphere [*Magde and Sparks*, 1997] to the western end of the segment, or is trapped in the deep lithosphere. The remainder, a small fraction of the total melt produced, forms thin crust and/or and irregular extrusive volcanic layer. As the lithosphere thins toward the western end of the segment more melt is able to reach shallow depths. This increases the abundance of hummocky volcanic terrain, and thickens the crust and magnetic source layer. The large distance (~40 km or more) at which the rift valley of segment DA-1 begins curving into the Andrew Bain reflects the strength of the lithospheric weld across the transform fault; it is entirely possible that the apparent obliquity of the rift valley at the eastern end of segment DA-1 is actually rift valley curvature produced by the weld. If this model is correct, the eastern end of segment DA-1 represents an unusual, if not unique, accre-

tionary regime: nonvolcanic accretion produced by a combination of ultraslow spreading and the cooling effect of a long-offset transform fault.

9. Andrew Bain Transform Fault: A Major Melt Supply Boundary

[62] The axial relief, MBA variation, and length of the western rift valley of segment DA-1 (i.e., the fully magmatic portion of the segment) are very similar to those of segments 11 and 14 near the Rodrigues Triple Junction (Table 1 and Figure 11). This observation, combined with large axial depth, suggests that segment DA-1 receives a relatively low volume of melt. The large relief and MBA amplitude of the segment are thus the result of strong melt focusing, which agrees with our previous analysis of seafloor textures and lithospheric thickness. As stated in section 8.2., it is reasonable to presume that segment DA-1 may be on the distal end of the gradient in mantle upwelling responsible for depth and MBA asymmetries within the 15.5°E–25°E supersegment [*Grindlay et al.*, 1998].

[63] We demonstrated above that segments AM-1 and MP-1 receive a high supply of melt, likely due to the influence of the Marion hot spot. Our observations thus allow us to fill the gap in the regional melt supply analysis of *Cannat et al.* [2008]. Segment DA-1 may be added to the 14.18°E–25.14°E intermediate-to-low melt supply region, and segments AM-1 and MP-1 may be added to the 35.55°E–41.53E° high melt supply region [see *Cannat et al.*, 2008, Table 1]. The Andrew Bain transform fault thus represents not only a large topographic boundary (profile in Figure 1), but a large melt supply boundary as well.

10. Conclusions

[64] 1. Within the two segments northeast of, and the one segment southeast of, the Andrew Bain transform fault, we observe similar asymmetries in seafloor texture, MBA amplitude, magnetization, and rift valley curvature. We interpret these asymmetries to reflect variations in (1) the amount of melt delivered to and emplaced along the ridge axis and (2) the subaxial lithospheric thickness, which controls the strength of the lithospheric welds responsible for rift valley curvature. Despite the observed similarities between the three segments, we argue that the asymmetries observed at either end of the Andrew Bain transform fault are not created by the same mechanism.

[65] 2. The two segments northeast of the Andrew Bain transform fault have high melt supply due to the proximity of the Marion hot spot. The asymmetries within these two segments result from channelized subaxial asthenospheric flow from the hot spot. In this model, partial melts entrained in the asthenospheric flow pool against the western bounding transform faults, producing thicker crust and a thicker extrusive layer in these areas relative to areas near the eastern bounding transform faults. The interaction of the hot subaxial flow with the thickening lithosphere at the western end of these segments heats and thins this lithosphere. This reduces the strength of the lithospheric weld and hence rift valley curvature.

[66] 3. An along-axis gradient in seafloor texture, from equal amounts of volcanic and nonvolcanic seafloor in the east to almost entirely volcanic seafloor in the west, reflects an east-west gradient in melt delivery in the segment southwest of the Andrew Bain transform fault. Rather than being a result of ridge obliquity, low melt delivery on the eastern end of this segment is likely due to the strong influence of the long-offset Andrew Bain transform fault. Extremely thick and cold lithosphere abutting the end of the segment thickens the subaxial lithosphere, strengthens the lithospheric weld and rift valley curvature, reduces melt production, and focuses melt to the west. This limits the amount of melt that reaches shallow levels to produce crust and extrusive volcanics.

[67] 4. The Andrew Bain transform fault represents a major melt supply boundary on the SWIR, separating a high melt supply region to the northeast from an intermediate-to-low melt supply region to the southwest.

Acknowledgments

[68] We thank Donna Blackman, Jeff Gee, Daniel Sauter, Graham Baines, and two anonymous reviewers for their helpful comments on the manuscript. This work was supported by National Science Foundation grant OCE-0329565.

References

Baines, A. G., M. J. Cheadle, H. J. B. Dick, A. H. Scheirer, B. E. John, N. J. Kusznir, and T. Matsumoto (2007), Evolution of the Southwest Indian Ridge from 55°45′E to 62°E: Changes in plate-boundary geometry since 26 Ma, *Geochem. Geophys. Geosyst.*, *8*, Q06022, doi:10.1029/2006GC001559.

Blackman, D. K., and D. W. Forsyth (1991), Isostatic compensation of tectonic features of the Mid-Atlantic Ridge: 25–27°

30′S, *J. Geophys. Res.*, *96*, 11,741–11,758, doi:10.1029/91JB00602.

Blackman, D. K., B. Ildefonse, B. E. John, Y. Ohara, D. J. Miller, C. J. MacLeod, and the Expedition 304/305 Scientists (2006), *Oceanic Core Complex Formation, Atlantis Massif, Proc. Integrated Ocean Drill. Program*, vol. 304/305, doi:10.2204/iodp.sp.304305.2004, Ocean Drill. Program, College Station, Tex.

Bown, J. W., and R. S. White (1994), Variation with spreading rate of oceanic crustal thickness and geochemistry, *Earth Planet. Sci. Lett.*, *121*, 435–449, doi:10.1016/0012-821X(94)90082-5.

Cande, S. C., and D. V. Kent (1995), Revised calibration of the geomagnetic polarity timescale for the Late Cretaceous and Cenozoic, *J. Geophys. Res.*, *100*, 6093–6095, doi:10.1029/94JB03098.

Cannat, M., C. Rommevaux-Jestin, D. Sauter, C. Deplus, and V. Mendel (1999), Formation of the axial relief at the very slow spreading Southwest Indian Ridge (49° to 69°E), *J. Geophys. Res.*, *104*, 22,825–22,843, doi:10.1029/1999JB900195.

Cannat, M., C. Rommevaux-Jestin, and H. Fujimoto (2003), Melt supply variations to a magma-poor ultra-slow spreading ridge (Southwest Indian Ridge 61° to 69°E), *Geochem. Geophys. Geosyst.*, *4*(8), 9104, doi:10.1029/2002GC000480.

Cannat, M., D. Sauter, V. Mendel, E. Ruellan, K. Okino, J. Escartin, V. Combiet, and M. Baala (2006), Modes of seafloor generation at a melt-poor ultraslow-spreading ridge, *Geology*, *34*, 605–608, doi:10.1130/G22486.1.

Cannat, M., D. Sauter, A. Bezos, C. Meyzen, E. Humler, and M. Le Rigoleur (2008), Spreading rate, spreading obliquity, and melt supply at the ultraslow spreading Southwest Indian Ridge, *Geochem. Geophys. Geosyst.*, *9*, Q04002, doi:10.1029/2007GC001676.

Carbotte, S. M., C. Small, and K. Donnelly (2004), The influence of ridge migration on the magmatic segmentation of mid-ocean ridges, *Nature*, *429*, 743–746, doi:10.1038/nature02652.

Caress, D. W., and D. N. Chayes (1996), Improved processing of Hydrosweep DS multibeam data on the R/V *Maurice Ewing*, *Mar. Geophys. Res.*, *18*, 631–650, doi:10.1007/BF00313878.

Chu, D., and R. G. Gordon (1999), Evidence for motion between Nubia and Somalia along the Southwest Indian Ridge, *Nature*, *398*, 64–67, doi:10.1038/18014.

Cochran, J. R., G. J. Kurras, M. H. Edwards, and B. J. Coakley (2003), The Gakkel Ridge: Bathymetry, gravity anomalies, and crustal accretion at extremely slow spreading rates, *J. Geophys. Res.*, *108*(B2), 2116, doi:10.1029/2002JB001830.

Debayle, E., B. Kennett, and K. Priestley (2005), Global azimuthal seismic anisotropy and the unique plate-motion deformation of Australia, *Nature*, *433*, 509–512, doi:10.1038/nature03247.

Detrick, R. S., H. D. Needham, and V. Renard (1995), Gravity anomalies and crustal thickness variations along the Mid-Atlantic Ridge between 33°N and 40°N, *J. Geophys. Res.*, *100*, 3767–3787, doi:10.1029/94JB02649.

Dick, H. J. B., et al. (2000), A long in situ section of the lower ocean crust: Results of ODP Leg 176 drilling at the Southwest Indian Ridge, *Earth Planet. Sci. Lett.*, *179*, 31–51, doi:10.1016/S0012-821X(00)00102-3.

Dick, H. J. B., J. Lin, and H. Schouten (2003), An ultraslow-spreading class of ocean ridge, *Nature*, *426*, 405–412, doi:10.1038/nature02128.

Dulaney, T. (2002), Volcanic morphology of the ultra-slow spreading Southwest Indian Ridge (15°–35°E): Implications for crustal construction, M.Sc. thesis, 203 pp., Univ. of N. C. at Wilmington, Wilmington.

Engdahl, E. R., R. van der Hilst, and R. Buland (1998), Global teleseismic earthquake relocation with improved travel time procedures for depth determination, *Bull. Seismol. Soc. Am.*, *88*(3), 722–743.

Fisher, R. L., and A. M. Goodwille (1997), The physiography of the Southwest Indian Ridge, *Mar. Geophys. Res.*, *19*, 451–455, doi:10.1023/A:1004365019534.

Fox, P. J., and D. G. Gallo (1984), A tectonic model for ridge-transform-ridge plate boundaries: Implications for the structure of oceanic lithosphere, *Tectonophysics*, *104*, 205–242, doi:10.1016/0040-1951(84)90124-0.

Fujita, K., and N. H. Sleep (1978), Membrane stresses near mid-ocean ridge-transform intersections, *Tectonophysics*, *50*, 207–221, doi:10.1016/0040-1951(78)90136-1.

Georgen, J. E., and J. Lin (2003), Plume-transform interactions at ultra-slow spreading ridges: Implications for the Southwest Indian Ridge, *Geochem. Geophys. Geosyst.*, *4*(9), 9106, doi:10.1029/2003GC000542.

Georgen, J. E., J. Lin, and H. J. B. Dick (2001), Evidence from gravity anomalies for interactions of the Marion and Bouvet hotspots with the Southwest Indian Ridge: Effects of transform offsets, *Earth Planet. Sci. Lett.*, *187*, 283–300, doi:10.1016/S0012-821X(01)00293-X.

Grindlay, N. R., P. J. Fox, and K. C. Macdonald (1991), Second-order ridge axis discontinuities in the South Atlantic: Morphology, structure, and evolution, *Mar. Geophys. Res.*, *13*, 21–49, doi:10.1007/BF02428194.

Grindlay, N. R., J. A. Madsen, C. Rommevaux, J. G. Sclater, and S. Murphy (1996), Southwest Indian Ridge 15°E–35°E: A geophysical investigation of an ultra-slow spreading mid-ocean ridge system, *InterRidge News*, *5*, 7–12.

Grindlay, N. R., J. A. Madsen, C. Rommevaux-Jestin, and J. G. Sclater (1998), A different pattern of ridge segmentation and mantle Bouguer anomalies along the ultra-slow spreading Southwest Indian Ridge (15°30′E to 25°E), *Earth Planet. Sci. Lett.*, *161*, 243–253, doi:10.1016/S0012-821X(98)00154-X.

Gripp, A. E., and R. G. Gordon (2002), Young tracks of hotspots and current plate velocities, *Geophys. J. Int.*, *150*, 321–361, doi:10.1046/j.1365-246X.2002.01627.x.

Hosford, A., M. A. Tivey, T. Matsumoto, H. J. B. Dick, H. Schouten, and H. Kinoshita (2003), Crustal magnetization and accretion at the Southwest Indian Ridge near the Atlantis II Fracture Zone, 0–25 Ma, *J. Geophys. Res.*, *108*(B3), 2169, doi:10.1029/2001JB000604.

Klein, E. M., and C. H. Langmuir (1987), Global correlations of ocean ridge basalt chemistry with axial depth and crustal thickness, *J. Geophys. Res.*, *92*, 8089–8115, doi:10.1029/JB092iB08p08089.

Klitgord, K. D. (1976), Sea-floor spreading: The central anomaly magnetization high, *Earth Planet. Sci. Lett.*, *29*, 201–209, doi:10.1016/0012-821X(76)90040-6.

Kuo, B. Y., and D. W. Forsyth (1988), Gravity anomalies of the ridge transform system in the South Atlantic between 31° and 34°: Upwelling centers and variation in crustal thickness, *Mar. Geophys. Res.*, *10*, 205–232, doi:10.1007/BF00310065.

Langel, R. A. (1992), International geomagnetic reference field: The sixth generation, *J. Geomagn. Geoelectr.*, *44*, 679–707.

Lemaux, J., R. G. Gordon, and J.-Y. Royer (2002), Location of the Nubia-Somalia boundary along the Southwest Indian

Ridge, *Geology*, *30*, 339–342, doi:10.1130/0091-7613(2002)030<0339:LOTNSB>2.0.CO;2.

Ligi, M., E. Bonatti, L. Gasperini, and A. N. B. Poliakov (2002), Oceanic broad multifault transform plate boundaries, *Geology*, *30*, 11–14, doi:10.1130/0091-7613(2002)030<0011:OBMTPB>2.0.CO;2.

Lin, J., G. M. Purdy, H. Schouten, J.-C. Sempéré, and C. Zervas (1990), Evidence from gravity data for focused magmatic accretion along the Mid-Atlantic Ridge, *Nature*, *344*, 627–632, doi:10.1038/344627a0.

Macdonald, K. C., S. P. Miller, S. P. Huestis, and F. N. Speiss (1980), Three Dimensional modeling of a magnetic reversal boundary from inversion of deep-tow measurements, *J. Geophys. Res.*, *85*, 3670–3680, doi:10.1029/JB085iB07p03670.

Macdonald, K. C., J.-C. Sempéré, and P. J. Fox (1984), East Pacific Rise from Siquieros to Orozco fracture zones: Along-strike continuity of axial neovolcanic zone and structure and evolution of overlapping spreading centers, *J. Geophys. Res.*, *89*, 6049–6069, doi:10.1029/JB089iB07p06049.

Macdonald, K. C., P. J. Fox, L. J. Perram, M. F. Eisen, R. M. Haymon, S. P. Miller, S. M. Carbotte, M.-H. Cormier, and A. N. Shor (1988), A new view of the mid-ocean ridge from the behaviour of ridge-axis discontinuities, *Nature*, *335*, 217–225, doi:10.1038/335217a0.

Madsen, J. A., R. S. Detrick, J. G. Mutter, P. Buhl, and J. A. Orcutt (1990), A two- and three-dimensional analysis of gravity anomalies associated with the East Pacific Rise at 9°N and 13°N, *J. Geophys. Res.*, *95*, 4967–4987, doi:10.1029/JB095iB04p04967.

Magde, L. S., and D. W. Sparks (1997), Three-dimensional mantle upwelling, melt generation, and melt migration beneath slow spreading ridges, *J. Geophys. Res.*, *102*, 20,571–20,583, doi:10.1029/97JB01278.

Magde, L. S., D. W. Sparks, and R. S. Detrick (1997), The relationship between buoyant mantle flow, melt migration, and the mantle Bouguer anomaly patterns observed along the MAR from 33°N to 35°N, *Earth Planet. Sci. Lett.*, *148*, 59–67, doi:10.1016/S0012-821X(97)00039-3.

Mahoney, J., A. P. Le Roex, Z. Peng, R. L. Fisher, and J. H. Natland (1992), Southwestern limits of Indian Ocean Ridge mantle and the origin of low $^{206}Pb/^{204}Pb$ mid-ocean ridge basalt: Isotope systematics of the central Southwest Indian Ridge (17°–50°E), *J. Geophys. Res.*, *97*, 19,771–19,790, doi:10.1029/92JB01424.

Mendel, V., D. Sauter, L. M. Parson, and J.-R. Vanney (1997), Segmentation and morphotectonic variations along a super slow-spreading center: The Southwest Indian Ridge (57° E–70° E), *Mar. Geophys. Res.*, *19*, 505–533, doi:10.1023/A:1004232506333.

Mendel, V., D. Sauter, C. Rommevaux-Jestin, P. Patriat, F. Lefebvre, and L. M. Parson (2003), Magmato-tectonic cyclicity at the ultra-slow spreading Southwest Indian Ridge: Evidence from variations of axial volcanic ridge morphology and abyssal hills pattern, *Geochem. Geophys. Geosyst.*, *4*(5), 9102, doi:10.1029/2002GC000417.

Meyzen, C. M., J. N. Ludden, E. Humler, B. Luais, M. J. Toplis, C. Mével, and M. Storey (2005), New insights into the origin and distribution of the DUPAL isotope anomaly in the Indian Ocean mantle from MORB of the Southwest Indian Ridge, *Geochem. Geophys. Geosyst.*, *6*, Q11K11, doi:10.1029/2005GC000979.

Montési, L. G. J., and M. D. Behn (2007), Mantle flow and melting underneath oblique and ultraslow mid-ocean ridges, *Geophys. Res. Lett.*, *34*, L24307, doi:10.1029/2007GL031067.

Parker, R. L. (1973), The rapid calculation of potential anomalies, *Geophys. J. R. Astron. Soc.*, *31*, 447–455.

Parker, R. L., and S. P. Huestis (1974), The inversion of magnetic anomalies in the presence of topography, *J. Geophys. Res.*, *79*, 1587–1593, doi:10.1029/JB079i011p01587.

Parker, R. L., and D. W. Oldenburg (1973), Thermal model and ocean ridges, *Nat. Phys. Sci.*, *242*, 137–139.

Phipps Morgan, J., and E. M. Parmentier (1984), Lithospheric stress near a ridge-transform intersection, *Geophys. Res. Lett.*, *11*, 113–116, doi:10.1029/GL011i002p00113.

Prince, R. A., and D. W. Forsyth (1988), Horizontal extent of anomalously thin crust near the Vema Fracture Zone from the three-dimensional analysis of gravity anomalies, *J. Geophys. Res.*, *93*, 8051–8063, doi:10.1029/JB093iB07p08051.

Reid, I., and H. R. Jackson (1981), Oceanic spreading rate and crustal thickness, *Mar. Geophys. Res.*, *5*, 165–172.

Ribe, N. M., U. R. Christensen, and J. Theißing (1995), The dynamics of plume-ridge interaction, 1: Ridge-centered plumes, *Earth Planet. Sci. Lett.*, *134*, 155–168, doi:10.1016/0012-821X(95)00116-T.

Rommevaux, C., C. Deplus, P. Patriat, and J.-C. Sempéré (1994), Three-dimensional gravity study of the Mid-Atlantic Ridge: Evolution of the segmentation between 28° and 29°N during the last 10 m.y., *J. Geophys. Res.*, *99*, 3015–3029, doi:10.1029/93JB02361.

Sandwell, D. T., and W. H. F. Smith (2009), Global marine gravity from retracked Geosat and ERS-1 altimetry: Ridge segmentation versus spreading rate, *J. Geophys. Res.*, *114*, B01411, doi:10.1029/2008JB006008.

Sauter, D., P. Patriat, C. Rommevaux-Jestin, M. Cannat, A. Briais, and the Gallieni Shipboard Scientific Party (2001), The Southwest Indian Ridge between 49°15′E and 57°E: Focused accretion and magma redistribution, *Earth Planet. Sci. Lett.*, *192*, 303–317, doi:10.1016/S0012-821X(01)00455-1.

Sauter, D., L. Parson, V. Mendel, C. Rommevaux-Jestin, O. Gomez, A. Briais, C. Mével, K. Tamaki, and the FUJI Scientific Team (2002), TOBI sidescan sonar imagery of the very slow-spreading Southwest Indian Ridge: Evidence for along-axis magma redistribution, *Earth Planet. Sci. Lett.*, *199*, 81–95, doi:10.1016/S0012-821X(02)00543-5.

Sauter, D., H. Carton, V. Mendel, M. Munschy, C. Rommevaux-Jestin, J.-J. Schott, and H. Whitechurch (2004a), Ridge segmentation and the magnetic structure of the Southwest Indian Ridge (at 50°30′E, 55°30′E and 66°20′E): Implications for magmatic processes at ultraslow-spreading centers, *Geochem. Geophys. Geosyst.*, *5*, Q05K08, doi:10.1029/2003GC000581.

Sauter, D., V. Mendel, C. Rommevaux-Jestin, L. M. Parson, H. Fujimoto, C. Mével, M. Cannat, and K. Tamaki (2004b), Focused magmatism versus amagmatic spreading along the ultra-slow spreading Southwest Indian Ridge: Evidence from TOBI side scan sonar imagery, *Geochem. Geophys. Geosyst.*, *5*, Q10K09, doi:10.1029/2004GC000738.

Sauter, D., M. Cannat, C. Meyzen, A. Bezos, P. Patriat, E. Humler, and E. Debayle (2009), Propagation of a melting anomaly along the ultraslow Southwest Indian Ridge between 46°E and 52°20′E: Interaction with the Crozet hotspot?, *Geophys. J. Int.*, *179*, 687–699, doi:10.1111/j.1365-246X.2009.04308.x.

Sclater, J. G., N. R. Grindlay, J. A. Madsen, and C. Rommevaux-Jestin (2005), Tectonic interpretation of the Andrew Bain transform fault: Southwest Indian Ocean, *Geochem. Geophys. Geosyst.*, *6*, Q09K10, doi:10.1029/2005GC000951.

Sempéré, J.-C., and K. C. Macdonald (1986), Deep-tow studies of the overlapping spreading centers near 9°N on the

East Pacific Rise, *Tectonics*, *5*, 881–900, doi:10.1029/TC005i006p00881.

Seyler, M., M. Cannat, and C. Mével (2003), Evidence for major-element heterogeneity in the mantle source of abyssal peridotites from the Southwest Indian Ridge (52° to 68°E), *Geochem. Geophys. Geosyst.*, *4*(2), 9101, doi:10.1029/2002GC000305.

Standish, J. J., H. J. B. Dick, P. J. Michael, W. G. Melson, and T. O'Hearn (2008), MORB generation beneath the ultraslow spreading Southwest Indian Ridge (9–25°E): Major element chemistry and the importance of process versus source, *Geochem. Geophys. Geosyst.*, *9*, Q05004, doi:10.1029/2008GC001959.

Tivey, M. A., and B. E. Tucholke (1998), Magnetization of 0–29 MA ocean crust on the Mid-Atlantic Ridge, 25°30′ to 27°10′N, *J. Geophys. Res.*, *103*, 17,807–17,826, doi:10.1029/98JB01394.

Tucholke, B. E., and J. Lin (1994), A geological model for the structure of ridge segments in slow spreading ocean crust, *J. Geophys. Res.*, *99*, 11,937–11,958, doi:10.1029/94JB00338.

Tucholke, B. E., M. D. Behn, W. R. Buck, and J. Lin (2008), Role of melt supply in oceanic detachment faulting and formation of megamullions, *Geology*, *36*, 455–458, doi:10.1130/G24639A.1.

Vogt, P. R., and G. L. Johnson (1975), Transform faults and longitudinal flow below the Midoceanic ridge, *J. Geophys. Res.*, *80*, 1399–1428, doi:10.1029/JB080i011p01399.

Wessel, P., and W. H. F. Smith (1998), New, improved version of the Generic Mapping Tools, *Eos Trans. AGU*, *79*(47), 579, doi:10.1029/98EO00426.

West, B. P., and J.-C. Sempéré (1998), Gravity anomalies, flexure of the axial lithosphere, and along-axis astheno-spheric flow beneath the Southeast Indian Ridge, *Earth Planet. Sci. Lett.*, *156*, 253–266, doi:10.1016/S0012-821X(98)00010-7.

White, R. S., T. A. Minshull, M. J. Bickle, and C. J. Robinson (2001), Melt generation at very slow-spreading oceanic ridges: Constraints from geochemical and geophysical data, *J. Petrol.*, *42*, 1171–1196, doi:10.1093/petrology/42.6.1171.